COLOR GENERATION AND ENHANCEMENT USING LARGE-SCALE COMPATIBLE METAMATERIAL DESIGN ARCHITECTURES

A DISSERTATION SUBMITTED TO
THE GRADUATE SCHOOL OF ENGINEERING AND SCIENCE
OF BILKENT UNIVERSITY
IN PARTIAL FULFILLMENT OF THE REQUIREMENTS FOR
THE DEGREE OF
DOCTOR OF PHILOSOPHY
IN
MATERIALS SCIENCE AND NANOTECHNOLOGY

By

Ali Cahit Köşger

Jan 2022

COLOR GENERATION AND ENHANCEMENT USING LARGE-SCALE COMPATIBLE METAMATERIAL DESIGN ARCHITECTURES

By Ali Cahit Köşger
Jan, 2022

We certify that we have read this dissertation and that in our opinion it is fully adequate, in scope and in quality, as a dissertation for the degree of Doctor of Philosophy.

_____

Ekmel Özbay (Advisor)

_____

Alpan Bek

_____

Oğuz Gülseren

_____

Talip Serkan Kasırga

_____

Haluk Külah

Approved for the Graduate School of Engineering and Science:

_____

Ezhan Karaşan
Director of the Graduate School

ABSTRACT

COLOR GENERATION AND ENHANCEMENT USING LARGE-SCALE COMPATIBLE METAMATERIAL DESIGN ARCHITECTURES

Ali Cahit Köşger
Ph.D. in Materials Science and Nanotechnology
Advisor: Ekmel Özbay
January 2022

Metamaterials are a type of artificial matt that can impose exotic functionalities beyond natural materials. These specifically designed sub-wavelength structures acquire these functionalities from their collective geometric arrangement rather than their individual single-unit properties. As a result, metamaterials have shown promising applications, including negative refraction, artificial magnetism, asymmetric transmission, lasing, and cloak of invisibility. Among all these applications, the concept of color generation and enhancement using metamaterial designs have attracted much attention in recent years.

We can achieve color generation from two primary sources: i) filtering white light, and ii) generating light from emitting materials such as quantum dots. In color generation using white light, a metamaterial design reflects or transmits a narrow portion of the incident spectrum. Thus, the design acts as a color filter. However, the source is already a narrowband color light in the second category. Thus metamaterials merely amplify the color intensity rather than manipulate its spectral response.

In this thesis, metamaterial structures are designed, fabricated, and characterized in both categories mentioned above; The content of this thesis consists of two parts;

i) In the first part, we generated additive red-green-blue (RGB) colors in reflectance mode with near-unity amplitude. For this purpose, we

designed a multilayer structure made of metal-insulator-metal-semiconductor-insulator (MIMSI) stacks to achieve >0.9 reflection peaks with full-width-at-half-maximum (FWHM) values $<0.3\lambda_{peak}$. The proposed design also shows near-zero reflection in off-resonance spectral ranges, which, in turn, leads to high color purity. Finally, we fabricated the optimized designs and verified the simulation and theoretical results with characterization findings. This work demonstrates the potential of multilayer tandem cavity designs in realizing lithography-free large-scale compatible functional optical coatings.

ii) In the second part, we utilized a large-scale compatible plasmonic nanocavity design platform to achieve almost an order of magnitude photoluminescence enhancement from light-emitting quantum dots. The proposed design is multi-sized/multi-spacing gold (Au) nano units that are uniformly wrapped with thin aluminum oxide (Al_2O_3) layer as a foreign host to form a metal-insulator-semiconductor (MIS) cavity, as we coated them with semiconductor quantum dots (QDs). Our numerical and experimental data demonstrate that, in an optimal insulator layer thickness, the simultaneous formation of broadband Fabry-Perot (FP) resonances and plasmonic hot spots leads to enhanced light absorption within the QD unit. This improvement in absorption response leads to the PL enhancement of QDs. This work demonstrates the potential and effectiveness of a host comprised of random plasmonic nanocavities in the realization of lithography-free efficient emitters.

Overall, this thesis presents an alternative perspective on applying large-scale compatible metamaterials in color generation. Furthermore, the proposed designs and routes can be extended toward other functional photoelectronic designs, where high performances can be acquired in scaleable architectures.

Keywords: Optical materials, metamaterials, color filter, light emission, quantum dot, plasmonics, scalable photonics

ÖZET

BÜYÜK ÖLÇEKLİ ÜRETİME UYGUN METAMALZEME TASARIM MİMARİSİ KULLANARAK RENK ÜRETME VE İYİLEŞTİRMESİ

Ali Cahit Köşger
Malzeme Bilimi ve Nanoteknoloji, Doktora
Tez Danışmanı: Ekmel Özbay
Ocak 2022

Metamalzemeler doğada bulunan malzemelerin ötesinde özel işlevlere sahip olacak şekilde tasarlanıp üretilen yapay malzemelerdir. Görünür ışık dalga boyundan daha küçük boyutlarda birimlerden oluşan bu malzemelerin karakteristik özellikleri her bir nano birimin spesifik fiziksel özellikleri ile beraber, nano birimlerin çeşitli geometrilerde yanyana durmaları ve birbirlerini etkilemelerinden ileri gelen toplu işlevler kazanmaları sayesinde oluşur. Metamalzemeler negatif kırılma indisi, yapay manyetizma, asimetrik geçirgenlik ve görünmezlik pelerini gibi pek çok ümit vadeden sıradışı uygulama imkanına sahiptir. Bu uygulamalar arasında renk üretimi, filtreleme ve iyileştirme işlevleri yakın zamanda dikkat çekici gelişmeler göstermiştir.

Renk üretimi temelde iki şekilde gerçekleşir: i) beyaz ışığın filtrelenmesi veya ii) belli dalga boyunda ışıma yapan Kuantum Nokta benzeri malzemeler sayesinde. Birinci yöntemde metamalzemeler üzerine düşen geniş bantlı beyaz ışığın sadece istenen dalga boyu aralığını geri yansıtarak renk oluşturur, bu bağlamda bir renk filtresi gibi davranır. İkinci yöntemde ışıma yapan madde zaten halihazırda tek bir renkte, küçük bir dalga boyu aralığında, ışık üretmektedir. Bu durumda metamalzemenin görevi renk tayfını değiştirmeden sadece bu ışımanın yoğunluğunu artırarak renk üretiminin iyileştirilmesidir.

Bu tezde yukarıda bahsedilen iki kategoride görev yapacak olan metamalzemele yapıları tasarlanmış, üretilmiş ve karakterize edilmiştir; dolayısıyla bu tezin içeriği iki kısıma bölünmüştür:

i) Birinci kısımda neredeyse yüzde yüz genliğe sahip eklemeli kırmızı-mavi-yeşil (RGB) renklerin yansıtma modunda üretimi gösterilmiştir. Bu amaçla çok katmanlı metal-yalıtkan-metal-yarıiletken-yalıtkan (MIMSI) istifleri tasarlanmış, yansıtma doruk değeri 0.9'dan büyük, yansıtma yarı-doruk genişliği $0.3\lambda_{peak}$'ten küçük malzemeler bu tasarımlarla başarılmıştır. Önerilen tasarım rezonans harici tayfta sıfıra yakın yansıtma değeri gösterdiğinden yüksek derecede renk saflığı elde edilmektedir. Optimize edilen tasarımlar üretilmiş, ve simülasyon hesapları ile üretim sonrası ölçümlerin tutarlı olduğu doğrulanmıştır. Bu çalışma belirli işlevlerde optik kaplamalar için çok katmanlı ardışık kavite tasarımlarının litografi olmaksızın, büyük ölçekli üretimi mümkün kıldığını göstermektedir.

ii) İkinci kısımda ışıma yapan kuantum noktaların ışıldanım (fotolüminesans) miktarını neredeyse on kat artıran bir plazmonik nanokavite tasarımının büyük ölçekli üretime uygun, litografi kullanmaksızın üretimi gerçekleştirilmiştir. Bu metamalzeme tasarımını gerçeklemek için farklı boyutlarda olan ve birbirlerinden farklı mesafelerde bulunan Altın nano birimlerin üzeri eşit şekilde ince bir aluminyum oksit (Al_2O_3) katman ile kaplanmış, aluminyum oksit katmanının üzerine ise Kuantum Noktaler serilmiştir. Böylece oluşan metal-yalıtkan-yarıiletken (MIS) kavite yapısı ışıma yapan Kuantum Noktalara konak vazifesi görmüştür. Yaptığımız nümerik hesaplamalar ve deneysel çalışmalar, optimum yalıtkan kalınlığı kullanıldığında, aynı anda hem geniş bantlı Fabry-Perot (FP) rezonansının hem de plazmonik sıcak noktaların oluşmasından dolayı, kuantum noktaların ışık emiliminin arttığını göstermiştir. Işık emiliminde oluşan bu artış neticede ışıldama (fotoluminesans) miktarının artmasına sebep olmaktadır. Bu çalışma büyük ölçekte ve litografi kullanılmadan üretilen rastgele plazmonik nanokavitelerin

verimli ışık kaynakları için konak olarak kullanılabilme potansiyelini göstermiştir.

Özetle, bu tez büyük ölçekli üretilebilir metamalzeme tasarımlarının renk üretimi için kullanılmasına alternatif bir bakış açısı sunmaktadır. Önerilen tasarım ve üretim yolları, başka işlevsel fotoelektronik aygıt tasarımları için de kullanılacak şekilde genişletilebilir. Bu yöntemler sayesinde yüksek performanslı fotoelektronik aygıtlar ölçeklenebilir mimarilerde tasarlanabilir.

Anahtar kelimeler: Optik malzemeler, metamalzemeler, renk filtreleri, ışık salınımı, kuantum noktalar, plazmonik, ölçeklenebilir fotonik malzemeler

Acknowledgment

First and foremost, I want to thank Bilkent University and all the people involved in its establishment, endowment, and continuous improvement up to this day. This thesis would not be possible without the institution, which has been the home for me for more than 10 years of my life. Secondly, I want to thank Prof. Dr. Ekmel Özbay, who has been an advisor and a mentor for me and is someone whom I look up to. Finally, I would like to thank my good friend and colleague Amir Ghobadi for his extensive help and guidance in executing the research on which this thesis has been based.

I thank my parents, Yavuz Selim Köşger and Fatma Köşger, who believed in me more than I believed in myself in completing my Ph.D. work at these trying times.

I thank my big sister Şule Betül Ülker for being ultra-supportive and kind and being a myriad of positivity for my life.

I thank my little brother Muhammed Bahadır Köşger for inspiring me to be realistic and rational and teaching me many valuable skills such as optimization and financial markets.

I thank my little sister Ayşe Serra Köşger, whom I believe will be an extraordinary scientist and achieve things beyond what I can dream of. Go girls in STEM!

Last but not least, I would like to thank my wife, Ayşe Sena Köşger -who had completed her thesis while raising 2 children- for her entire joyful existence that made my days glow. She ushers away all sorrows of life and gives me a reason to persevere. I also would like to thank my sons Yavuz Selim and Ahmet Rauf, for whom I pray that they eclipse the giants whose shoulders academia stands on and mature as human beings, as my father before me prayed for me to have “two wings” to fly.

CONTENTS

LIST OF FIGURES

CHAPTER 1. GENERAL INTRODUCTION

In the last decade, intensive investigations in the field of metamaterial-based perfect absorbers have focused on light confinement and harvesting in sub-wavelength design dimensions. Metals can show broad and narrowband light-matter interaction at sub-wavelength dimensions if the right material and arrangement are used[1]. This intense light-matter interaction is accomplished by either inter-band transitions or excitation of localized surface plasmon resonance (LSPR), which results from the collective oscillation of free conduction electrons. However, the fabrication of plasmonic nano units needs difficult and large-scale incompatible methods as lithography-based steps that require many years of expertise on expensive and delicate laboratory equipment, consequently limiting their scalability. As a result, recently, lithography-free metamaterial absorbers have received much interest [2], [3]. Planar multilayer designs are the most frequent kind of these scalable metamaterial absorbers, using Fabry-Perot (FP) resonance modes as the dominating absorption mechanism [2]. The most popular cavity absorber designs are based on metal-insulator-metal (MIM), metal-insulator-metal-insulator (MIMI), and periodic $(MI)_N$ pair-based cavity designs. Researchers also achieved light absorption in ultrathin absorbing layers using one-dimensional photonic crystal (1D-PC) designs. Nanostructured absorbers may outperform planar solutions where both a large active surface area and strong absorption are required. Researchers developed several novel synthesis routes to fulfill this demand. Examples of these approaches include deposition-induced structuring [4], [5], dewetting-based nano unit creation [6]–[8], oblique angle deposition [9]–[14], direct laser writing [15], and template-assisted etching [16], [17], and deposition [18], [19]. Besides the importance of the route, the selection of material is also an important aspect of lithography-free metamaterial absorber design. Figure 1 depicts the most suitable materials for constructing lithography-free absorber designs [2].

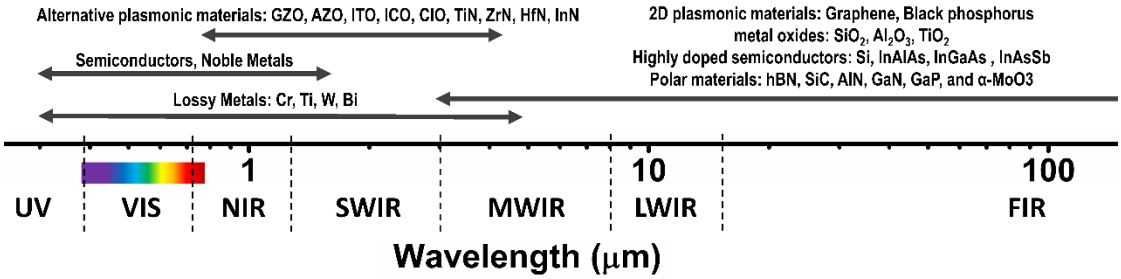

Figure 1.1 Possible absorber materials for the realization of LFMAs in different portions of the optical spectrum. (Reprinted with permission from Wiley Ref. [2]).

1.1. Thesis Goals

Our motivation in this Doctoral Thesis is to implement metamaterial and plasmonic design structures to generate and intensify high purity colors. For this purpose, we follow two pathways; i) generation of high purity and high-efficiency additive red-green-blue (RGB) colors from white light, using correctly designed planar multilayer color filters, ii) coupling of a plasmonic nano design into light-emitting quantum dot material to amplify the generated color signal.

1.2. Thesis Outline

The organization of this thesis is as follows:

Chapter 1 provides a general introduction to the concept of lithography-free metamaterial absorbers by highlighting the materials and routes needed for this application. Then it summarizes the thesis goals and outlines.

Chapter 2 provides a general overview of the scientific background of this work. It provides a literature review on recent studies on this topic. Afterward, we provide two theoretical sections; i) the optical interference in planar multilayer absorbers and ii) light-matter interaction in plasmonic nano units. Transfer matrix method (TMM) based modeling is utilized to find the optimal absorber material to achieve a near-perfect absorber used in color filter design.

Chapter 3 provides a detailed description of the characterization and measurement methods conducted in this dissertation, including structural, spectroscopic, and optical methods.

Chapter 4 presents the planar multilayer color filter's design, fabrication, and characterization. In addition, this chapter summarizes our achievements in realizing high-efficiency reflective RGB colors using an FP-based tandem shape cavity structure.

Chapter 5 presents our plasmonic enhanced quantum dot emission design using a lithography-free metamaterial scaffold. The proposed design is fabricated and characterized. Moreover, we evaluate the physical mechanism behind this enhancement using numerical simulation modelings.

Chapter 6 summarizes the achievements of this current Ph.D. thesis work and highlights the future routes and directions for follow-up studies.

CHAPTER 2. SCIENTIFIC BACKGROUND

2.1. Lithography-free Metal-based Metamaterial Perfect Absorbers

The main responsible mechanisms for light absorption in nanostructured metals are the collective oscillation of conduction electrons, so-called localized surface plasmon resonances (LSPRs), and inter-band transitions. The large wave-vectors of surface plasmons help confine EM fields into geometries much smaller than the light wavelength in vacuum, and these light confinement in ultrasmall volumes (or so-called hot spot formation) offer the possibility of light manipulation beyond the diffraction limit. But, this is not the only application of these hot spots. Upon excitation of LSPR in nanometals, the non-radiative decay of this resonance could lead to the formation of “hot carriers”[20], [21]. If these carriers have enough energy to path the Schottky barrier, formed in the metal-semiconductor interface, they can generate photocurrent[22], [23]. In recent years, plasmonics found promising applications as single-molecule level probing[24], [25], sensing[26], guiding[27], lasing[28], and color generation[29], the hot electron based photoconversion systems including photovoltaics (PV)[30], photodetector (PD)[31], and photoelectrochemical (PEC) cells[32]. However, the fabrication of these nano units requires complex and high-cost methods. Thus, as a solution to the scalability problem, the concept of lithography-free metamaterials has gained much momentum. The most commonly used designs in lithography-free metamaterials are planar multilayer structures. However, scientists have also explored nanostructured morphologies to realize nano units on large scales with feasible costs along with these planar designs.

The progress in most nanophotonic designs occurs with advancements in nanotechnology top-down and bottom-up fabrication routes. The commonly used fabrication tool for realizing these nano units is electron beam lithography (EBL). However, this technique is a complex, high-cost, and nonscalable approach. Although nanoimprint lithography (NIL) can pattern nano units in large areas, this process is also high-cost and complex due to difficulty in fabricating masks and sensitive processes required to apply masks. Moreover, the fabrication of densely packed, high-aspect-ratio nanostructures such as nanorods and nanowires is challenging with the NIL technique. Bottom-up

approaches can be adopted to obtain two-dimensional (2D) and three-dimensional (3D) designs, but these techniques also have a material limitation. Therefore, finding a large-scale compatible, lithography-free fabrication sequence with no material restriction could be groundbreaking. In the last years, scientists have developed different approaches to achieve this goal[6]–[8], [11], [33]–[38]. One of the common routes is based on dewetting ultrathin metal layers in a high vacuum level (to avoid transformation from metal to metal oxide) to form metal nano units. We anneal the metal to a temperature nearing its bulk melting point in this approach. When it reaches near melting point, the ultrathin planar layer deforms to minimize its surface tension, resulting in nanoscale islands of metal. Changing the parameters of dewetting temperature, dewetting duration, and the rate of heating/cooling, we can obtain a wide variety of shapes and forms of nano units. If the dewetting temperature is significantly below the bulk metal melting point, nano holes (NHs) with large inter-distances appear to form on the film. Increasing the dewetting duration results in larger NHs. Higher rates of heating/cooling at a higher temperature (but still below the melting point) can lead to the formation of denser NHs. The same processes can be adopted to acquire nanospheres (NSs). To form NSs higher temperatures, that are very close to the melting temperature of the bulk metal are required. By tuning the temperature, while keeping the other parameters the same, we can obtain small and sparse, or dense NSs. Increasing the temperature to a value above the metals melting point while keeping the dewetting duration short can lead to large and dense NSs. Increasing the metal film thickness triggers the synthesis of larger nanoparticles (NPs), and the same change of parameters can be applied to control the density of the NPs. Because most metals show strong light-matter interaction in such dimensions, we can utilize this method to cost-effectively produce meta-surfaces that manipulate the spectral response and broadness of the absorption. The variety of size, shape, and spacing of these nano units can excite multiple LSPRs modes whose superposition leads to a broadband light absorption that can encompass a large portion of the solar spectrum. Ultimately, coating these nano units with a thin planar layer can create a multi-thickness surface texture with overall continuity. Coating nano units uniformly is essential for applications such as PDs and PVs, where a continuous layer is required for an electron to transport through it. To move from these 2D designs to 3D nanostructures, the oblique angle deposition technique, which is a physical vapor deposition tool, can be employed. In this approach, we place the

sample and the deposition source in a specific geometry that makes the sample surface stay at an oblique angle to the direction of evaporated atoms. Upon incidence of the evaporated flux on the substrate surface, we introduce an additional factor that manages the arrangement of the atoms and results in the formation of nanostructured units rather than a continuous film. Based on theoretical explanations, this mechanistic factor, which controls the film's morphology, is called the atomic “shadowing effect.” The formation of nano nuclei prevents the deposition of incoming atoms in regions behind (i.e., shadowed regions). Our group has successfully demonstrated the usefulness of this method for the realization of ultra-broadband absorber designs in the mid-infrared (MIR) range of spectrum using indium doped tin oxide (ITO). We showed that using oblique angle deposition, we can make tightly packed ITO nanorods where multi-dimensional ultra-small gaps can trigger multiple plasmonic modes, and the superposition of multiple resonant modes causes an overall ultra-broadband MIR light harvester[11]. A similar setup was adopted to achieve Bismuth nano islands and nanorods on a thick planar Bismuth surface. We can control the length of these 3D nanostructures with the duration of deposition, where a longer deposition time leads to higher aspect ratios. To control the density and the distances between these 3D designs, we can combine the dewetting process with oblique angle deposition, where a pre-patterned dewetted sample defines the initial morphology (i.e., growth nuclei) of the structure. With oblique angle deposition, 3D lossless scaffolds with a large scattering cross-section can host an ultrathin metal shell layer. In this way, we can achieve a strong light-matter interaction in sub-wavelength thicknesses [37]. We demonstrate that this nanostructure can act as a lossy antenna with the ability to excite multiple longitudinal LSPR modes.

This thesis utilizes planar and oblique angle deposited configurations to realize lithography-free metamaterial designs. The following section provides a literature survey on recently developed lithography-free metamaterials. Then we present theoretical modeling to find the ideal conditions to realize a spectrally selective absorber. The sub-wavelength MIM nanocavity is the most widely researched planar-based design that achieves complete light absorption [39]–[46]. In this configuration, the top metal film is made of nano units, while the bottom mirror is a continuous reflecting mirror that reflects the whole visible spectrum. In the resonance condition, the light gets confined within the cavity, and consequently, this leads to perfect light absorption in dimensions

considerably smaller than the incident light wavelength. Scientists can harness the light in the required frequency range by coupling it into LSPR modes [39], [46]. Since LSPRs have limited spectral coverage, the operation bandwidth (BW) of these plasmonic absorbers covers a narrow spectral range [41], [43], [47]–[62]. We use various design techniques to expand the absorption BW of these MIM plasmonic nanocavities. The implementation of multi-size/multi-shape units as the top absorber layer, in which every unit has different absorption resonance and shape and superposition of these multiple LSPR modes lead to light absorption in a broad spectral range or BW, is one of the most widely used ideas[42], [63]–[70]. Alternative routes to realize plasmonic broadband metamaterial absorbers include utilizing tightly packed arranged lossy metal units, elongated geometries with the ability to excite dual/multi-band LSPR modes, and shapes with sharp edges[71]–[76]. However, the fundamental disadvantage of these design combinations is their high cost and large scale incompatible nature. As already said, EBL is necessary to produce the top sub-wavelength nano units, which is intrinsically an incompatible method for upscaling. Although nanoimprint lithography (NIL) is a possible alternative for up-scaling these samples, it is also a complicated and expensive method. As a result, to tackle these issues, the area of lithography-free metamaterial absorbers has attracted intensive attention as a way to bring these perfect absorbers to practical applications on large scales [6], [7], [77]–[103]. Non-resonant MIM cavities consisting of lossy metals such as chromium (Cr), titanium (Ti), tungsten (W), and nickel (Ni) can be employed to achieve perfect light absorption in the visible (Vis) and near-infrared (NIR) wavelength regimes, which is much stronger performance compared to noble metals [8], [93]. Using lossy metals as the top layer provides a low quality factor (QF) nanocavity that satisfies impedance matching condition criteria in an ultra-broadband frequency range. The use of noble metals like gold (Au) and silver (Ag) in this planar structure might result in narrow absorption BW, which is the reason why researchers make color filters using these types of metals rather than lossy ones [78], [83], [86], [88], [89], [91]. All in all, it is essential to know which material and configurations are needed to make perfect absorbers. This thesis uses both planar multilayer and plasmonic platforms, and we provide a general overview of the operation principle of ideal planar absorbers and plasmonic designs.

2.1.1. Theoretical Modellings

This subsection explains the theory behind metamaterial perfect absorbers by electromagnetically modeling the metamaterials in the numerical domain and solving Maxwell's equations using these models.

2.1.1.1. Planar Cavity Absorber

A numerical modeling method, called the transfer matrix method (TMM), is adopted for a multilayer $M(IX)_N$ pair-based cavity design to find the ideal permittivity values needed to achieve perfect light absorption (near zero reflection) in a specific range. The comprehensive design geometry used in this analysis is shown in Figure 2.1.

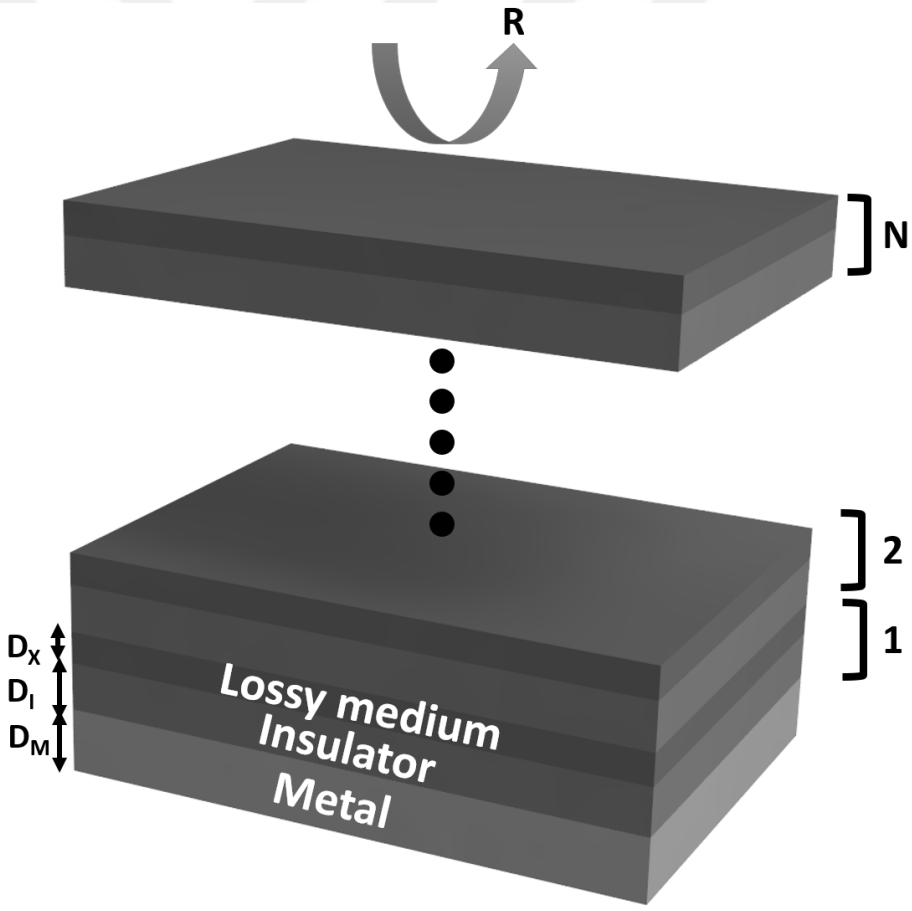

Figure 2.1. The design architecture we utilized in the TMM modeling investigations.

The bottom layer is a thick reflector metal layer in this general design. Using the TMM approach, we extract the permittivity values needed for near-zero reflection. M, I, and X stand for bottom metal, insulator, and absorbing medium in the proposed schematic. We should mention that the absorbing medium could be any type of lossy material, including metals and semiconductors. Using the TMM method, we extract the ideal permittivity for the lossy layers (ε_X) to achieve near-zero reflection in a specific wavelength value. In our analysis, we assume that the design is bound with air with a permittivity of ε_a and a substrate with a constant permittivity of ε_s. Considering $z = 0$ plane as the interface of air the first insulator layer, we can write the y component of the magnetic field as:

$$H_y(z) = \begin{Bmatrix} A_i e^{ik_a z} + A_r e^{-ik_a z}, z < 0 \\ I_{11} e^{ik_I z} + I_{12} e^{-ik_I Z}, 0 < z < D_I \\ X_{11} e^{ik_X (z-D_I)} + X_{12} e^{-ik_X (z-D_I)}, D_I < z < (D_I + D_X) \\ I_{21} e^{ik_I [z-(D_I+D_X)]} + I_{22} e^{-ik_I [z-(D_I+D_X)]}, (D_I + D_X) < z < L \\ . \\ . \\ . \\ M_{11} e^{ik_M [z-NL]} + M_{12} e^{-ik_M [z-NL]}, NL < z < (NL + D_M) \\ S_t e^{ik_s [z-(NL+D_M)]}, z > (NL + D_M) \end{Bmatrix} \quad (1)$$

Where,

$$L = 2D_I + D_X$$

and,

$$k_{j=(a,X,I,M,s)} = \sqrt{\varepsilon_j \omega^2 / c^2 - k_x^2}.$$

In these formulations, D_I, D_X, and D_M are the thicknesses of the dielectric, lossy medium, and bottom metal reflector layers, respectively. c is the speed of light in vacuum, k is the wave vector inside different media, and ε is the permittivity data of different layers. Applying the boundary conditions for transverse magnetic (TM) polarization (the continuity of the fields and their derivatives at the boundaries separating different media), the reflection of the incident light from the structure can be obtained[104] as:

$$R = |F_{12}/F_{11}|^2$$

Here,

$$F = \begin{bmatrix} F_{11} \\ F_{12} \end{bmatrix} = a^{-1}(X_1 X_2^{-1} I_1 I_2^{-1})^N M_1 M_2^{-1} s$$

where

$$a = \begin{bmatrix} 1 & 1 \\ ik_a/\varepsilon_a & -ik_a/\varepsilon_a \end{bmatrix}, s = \begin{bmatrix} 1 \\ \frac{ik_s}{\varepsilon_s} \end{bmatrix} \text{ (2a)}$$

$$I_1 = \begin{bmatrix} 1 & 1 \\ ik_I/\varepsilon_I & -ik_I/\varepsilon_I \end{bmatrix}, I_2 = \begin{bmatrix} e^{ik_I D_I} & e^{-ik_I D_I} \\ ik_I e^{ik_I D_I}/\varepsilon_I & -ik_I e^{-ik_I D_I}/\varepsilon_I \end{bmatrix} \text{ (2b)}$$

$$X_1 = \begin{bmatrix} 1 & 1 \\ ik_X/\varepsilon_X & -ik_X/\varepsilon_X \end{bmatrix}, X_2 = \begin{bmatrix} e^{ik_X D_X} & e^{-ik_X D_X} \\ ik_X e^{ik_X D_X}/\varepsilon_X & -ik_X e^{-ik_X D_X}/\varepsilon_X \end{bmatrix} \text{ (2c)}$$

$$M_1 = \begin{bmatrix} 1 & 1 \\ ik_M/\varepsilon_M & -ik_M/\varepsilon_M \end{bmatrix}, M_2 = \begin{bmatrix} e^{ik_M D_M} & e^{-ik_M D_M} \\ ik_M e^{ik_M D_M}/\varepsilon_M & -ik_M e^{-ik_M D_M}/\varepsilon_M \end{bmatrix} \text{ (2d)}$$

We use this modeling approach to design a color filter using a tandem shape FP cavity metamaterial. The idea is to design two-cavity absorbers in an integrated configuration. One of these cavities absorbs the short wavelength regime, while the other cavity is responsible for the longer wavelength ranges. So, the range between these two peaks is the only spectral part of the reflection. In this way, we produce RGB colors with high efficiency in the reflection mode. There are more details in the upcoming chapter.

2.2. Light-matter Interaction in Vicinity of Plasmonic Nanounits

Sub-wavelength nano-sized noble metals including gold (Au) and silver (Ag) nanoparticles can absorb visible light via excitation of LSPR (in a frequency adjacent to the natural oscillation frequency of the nano metal) [105]–[107]. However, besides the light-harvesting capability of these nano units, they can impose strong localized electric field amplification at the surface to intensify the light-matter interaction in their vicinity. Generally speaking, LSPR has two pathways to decay: i) radiatively and ii) non-radiatively, as seen in Figure 2.2. In the former case, the plasmonic nano unit emits photons due to the radiative decay process, and this radiation propagates isotropically in the space. Contrarily, the non-radiative process can yield the creation of hot carriers. These hot electrons/holes are created predominantly by electron-electron

scattering during the non-radiative relaxation process, resulting in inter-band and intra-band excitation of the conduction electrons. The creation of hot carriers occurs during non-radiative decay, and these carriers can subsequently transfer to an adjacent semiconductor in the Schottky junction with the metal layer. However, this thesis work mainly focuses on the radiative decay process, where plasmonic hot spots with strong near-field intensities amplify the emission of a neighboring quantum dot.

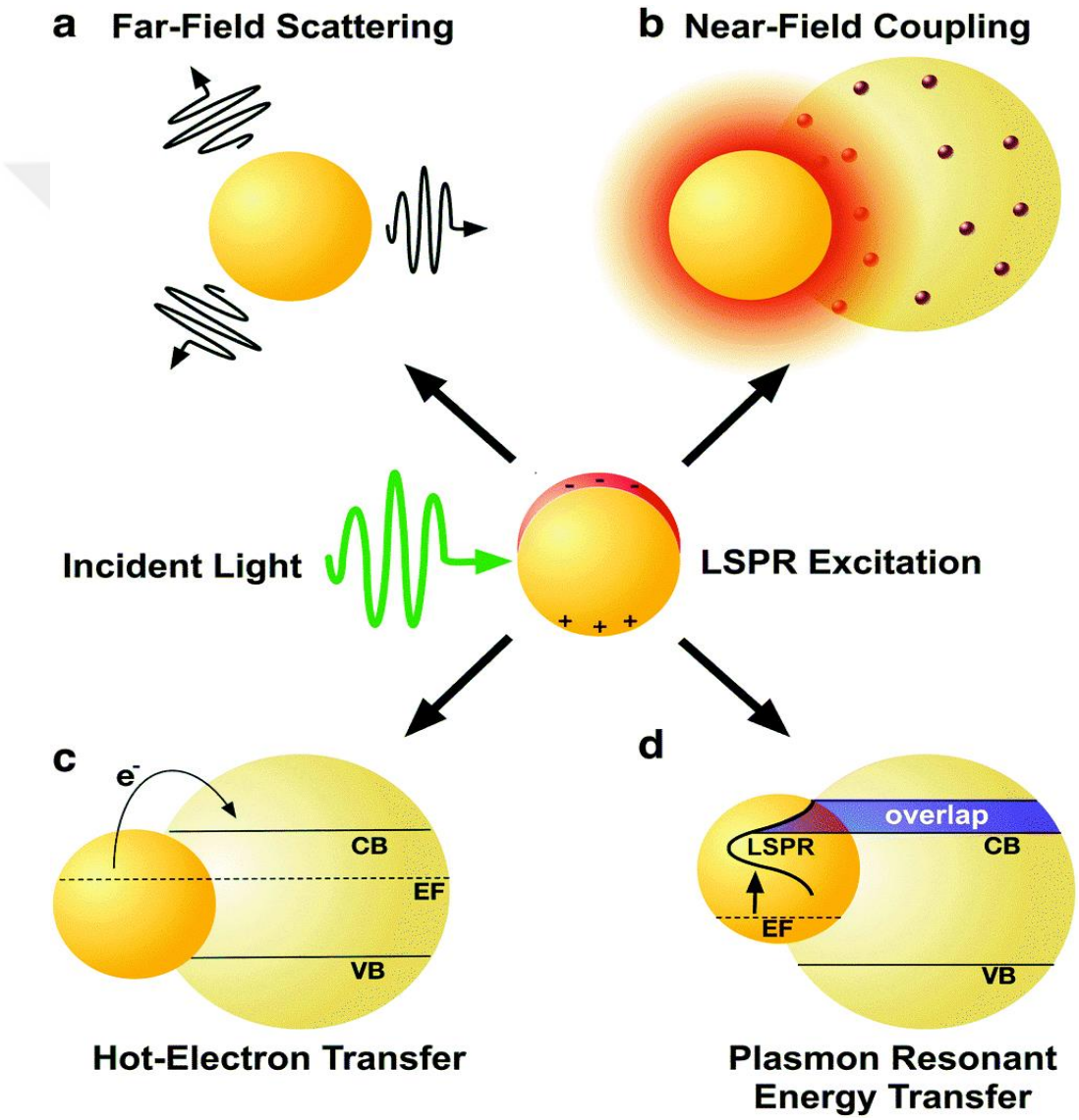

Figure 2.2 The LSPR driven energy transfer mechanisms in a plasmonic nano unit. The energy transfer to the semiconductor layer can occur through two main radiative processes, including (a) far-field scattering and (b) near-field coupling. The non-

radiative transfer process occurs via (c) hot electron transfer or (d) plasmon resonant energy transfer.

In the radiative energy transfer process, the plasmonic particle works as a nanoantenna, in which the LSPR relatively decays and transfers its energy via photon emission. Borrowing concepts from antenna terminology, we can categorize radiated electromagnetic power into 1) electromagnetic (EM) wave propagation in the far-field and 2) evanescent mode coupling in the near field. The first phenomenon is light scattering, where the plasmonic unit reradiates/reflects incoming photons. For the second phenomenon, the underlying mechanism is optical coupling (or near-field light confinement) which is the primarily responsible mechanism for enhancing interaction between light and matter in metal-semiconductor nanocomposites. Therefore, understanding these two processes' nature, differences, and conditions is essential in plasmonic design applications.

Scattering. When light illuminates a sub-wavelength particle, the incident electromagnetic field couples with the charged particles in atomic structure, leading to electrons beginning to vibrate. The vibration of electrons may result in secondary radiation known as scattering. On the other hand, absorption involves converting the incoming solar energy to another type of energy, such as heat. In general, we use a term called absorption/scattering cross-section with a unit of m^2 to analyze a system's absorption or scattering capability. We can compute the scattering cross-section by dividing the integrated total scattered power by the incoming light intensity. We can control this factor by changing the dimension of the plasmonic nanoparticle.

We use the following formula to determine scattering and absorption cross-sections in dimensions considerably lower than the incident wavelength [108], [109]:

$$\sigma_{abs} \approx \sigma_{ext} = k\, Im(\alpha) = 4\pi k R^3\, Im\left(\frac{\varepsilon_p - \varepsilon_m}{\varepsilon_p + 2\varepsilon_m}\right) \quad (3)$$

$$\sigma_{sca} = \frac{k^4}{6\pi}|\alpha|^2 = \frac{8\pi}{3}k^4 R^6 \left|\frac{\varepsilon_p - \varepsilon_m}{\varepsilon_p + 2\varepsilon_m}\right|^2 \quad (4)$$

Where k is the wavenumber, R is the particle radius, and ε_m is the system's complex permittivity. As this formula suggests, the scattering cross-section has

a direct relation with the 6th order of the particle size (R^6), while this dependence for the absorption cross-section is R^3. Generally, in radius values smaller than 50 nm ($R < 50\,nm$), the scattering cross-section is much smaller than its absorption one. As a result, absorption is the most crucial factor impacting the system's total optical performance in a plasmonic NP. For NP diameters larger than 100 nm, the scattering cross-section considerably dominates the absorption cross-section. Thus, far-field radiation (or scattering) is the dominant energy transfer process in large particles with dimensions comparable with incident light wavelength. Furthermore, in most plasmonic units, the calculated scattering cross-section is comparatively larger than the geometrical cross-sectional area of the particle. For example, the scattering cross-section of Ag NPs in the air is roughly an order of magnitude greater than the geometric cross-sectional area when the incoming light frequency is close to the resonance frequency of the particle. That is the fundamental reason why dispersion of all incoming light may be possible by a partial covering of metal nanoparticles on a background substrate with a filling fraction considerably smaller than unity[109], [110].

Optical near-field coupling. Near-field coupling originates from evanescent modes in the vicinity of the nanoparticle is the other radiative energy transfer mechanism. Different from propagating modes, evanescent modes do not carry energy. Thus, they can generate intense electric field amplitudes without violating energy conservation. The decaying short-range LSPR modes generate near-field evanescent modes or hot spots. A hot spot is an ultrasmall volume where light is concentrated. Many plasmonic nanostructure applications operate based on the presence of these hot spots. The distribution of electric fields around a plasmonic nano structure directly results from its geometric arrangement. The shape modifies the spectral location of the resonant peak and the amplitude of the near field electric field. Figure 2.3a compares the near field enhancement of various nanosphere, nanorod (NR), nanowire (NW), and nanopallet shapes where all of the nanoparticles have the same volume [111]. The field enhancement is the smallest in the pallet and sphere shapes, as seen in figure 2.3a.

Furthermore, for the case of nano pallets and nano spheres, the resonant peak's spectral location is in the ultraviolet range, which covers a small portion of solar irradiation (just 3%). Therefore nano sphere and nano pallet designs

can be considered not very useful for applications that require the interaction of light in the whole solar spectrum. However, elongated shapes such as NR and NW have different responses. The amplitude of field enhancement and resonance peak positions improve as the longitudinal-lateral dimensions difference increases, allowing for excellent light-harvesting in the visible and NIR domain. However, hot spots can also form at nanoparticles' sharp corners and edges[112][113].

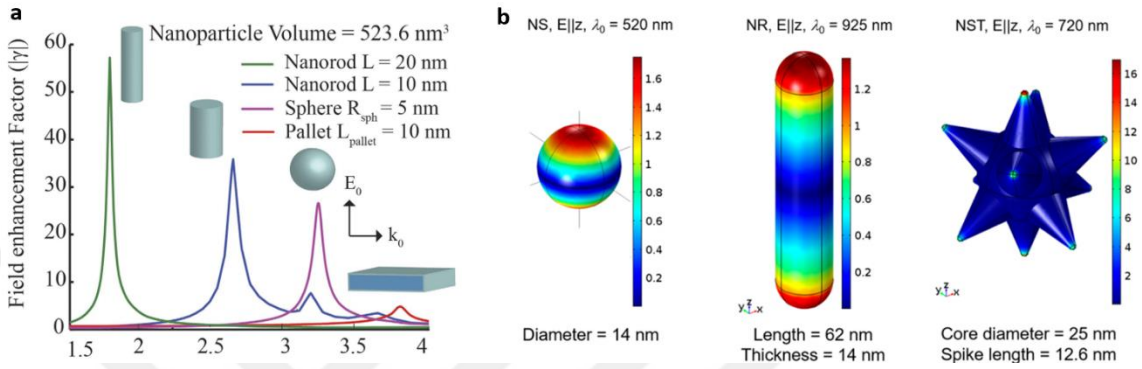

Figure 2.3 (a) The field enhancement factor as a function of light energy for different shaped plasmonic units. (b) The field distribution and amplitude on different plasmonic shapes.

We can demonstrate nanostars have ideal hot spot formation, as illustrated in Figure 2.3b, where we can achieve an electric field enhancement of an order of magnitude greater than that of a NW design. We can also predict that we can attain enhancement of similar magnitude in small gaps between metal NP clusters. We can also spatially control where these hot spots occur by controlling the shape and distribution of nanoparticles. Such high-intensity fields may increase the electronic transition probabilities for atoms or molecules exposed to them. In other words, the absorption cross-section of these micro resonant units is quite large. Consequently, we can predict that a relatively large concentration of electrons and holes would arise if a quantum dot were in the vicinity of such hot spots.

We assess that in a scenario where we use plasmonic nanoparticles for increasing emission rate from a quantum dot, the ideal configuration would be an array of near-touching plasmonic nanounits, where we bound the light in small gaps and confinement is significantly more efficient. However, the

realization of such small gaps is a fabrication challenge. This thesis adopts a fabrication route to synthesize near-touching plasmonic units on large scales.

CHAPTER 3. CHARACTERIZATION METHODS AND INSTRUMENTATION

In this thesis, we first designed the nano structures geometrically and calculated the expected behavior of these nano structures in the electromagnetic domain using FDTD numerical simulations. If the simulation results show desired behavior, we then proceed into the fabrication step. Otherwise, we reiterated the design based on simulation results and optimized the geometrical factors to obtain an efficient optical response. After reaching an optimized design solution, we employed various fabrication techniques and structural/optical characterization methods to verify the numerically calculated behavior. If we succeed in verifying simulation results, we consider the process is complete. Otherwise, we go back to step one.

In this chapter, we present an overview of various simulation, fabrication, and characterization methods and the theoretical calculations behind them to comprehend the results of the measurements. We carried out all the experiments and characterization studies at NANOTAM and UNAM, Bilkent University laboratories.

3.1. Numerical simulations

This section explains numerical calculation methods, material analysis, and data fitting employed in the design optimization cycle. This section is categorized as follows;

3.1.1. Simulation Domain

Figure 3.1 depicts the simulation setup. We employed Lumerical FDTD Solutions for this project. When compared to frequency domain finite element solvers, which need to conduct separate simulations in every wavelength value, FDTD has the advantage of performing simulations in a broad frequency range during a single run. As the name implies, this characteristic is particularly significant in designing ultra-broadband optical systems. Furthermore, as Figure 3.1a shows, we performed the simulations in a unit cell design with

boundary conditions on all 6 surfaces of the unit cell, which we explain in the upcoming subsections.

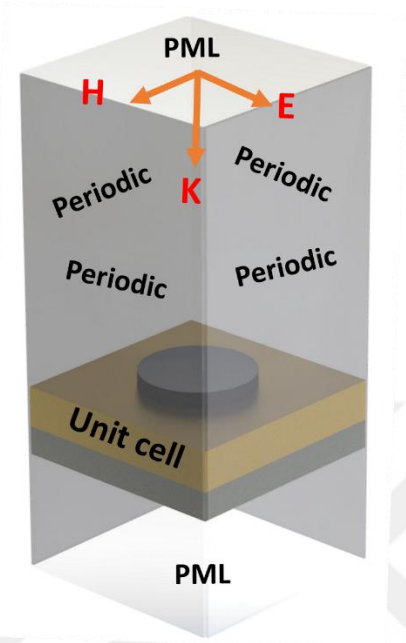

Figure 3.1 (a) The simulation setup used in our designs.

3.1.2. Boundary Conditions

The unit cell in our FDTD simulations is rectangular with six faces in three different Cartesian coordinates of x,y, and z. We adopt a proper boundary condition for every face before starting the simulation run. Before explaining this boundary condition assignment, we first need to look at different possible boundary conditions in an FDTD simulation region. In total, the Lumerical FDTD Solutions library has six different boundary conditions as follows;

***Perfectly matched layer (PML)*:** This boundary condition provides no reflection throughout the simulation spectrum. The term "perfectly matched layer" stems from this region's being composed of impedance-matched boundaries with no reflection of incoming broadband light. This boundary condition numerically simulates the walls of an anechoic chamber in an antenna measurement setup. The boundary absorbs the incoming electromagnetic wave and does not reflect it back into the region of the simulation domain. This

anti-reflection feature is due to putting up numerous (usually 8 to 10) layers on the surface's outer section, each with increasing dissipation. In summary, PML matches air into a lossy air with near-zero reflection property.

Metal or Perfect Electric Conductor (PEC): This boundary condition model a perfect electric conductor surface. We can deduce from Maxwell's Equations that for this boundary condition to be valid, the magnetic field component perpendicular to the surface and the electric field component parallel to the surface must be zero.

Perfect Magnetic Conductor (PMC): This boundary condition is the magnetic equivalent of the PEC boundary condition. A complete reflection occurs when the electromagnetic wave's magnetic field component parallel to the surface and the electric field component perpendicular to the surface are both zero. It's worth noting that, whereas the PEC boundary condition can be empirically verified to a large extent using metals, the PMC boundary condition cannot.

Periodic Boundary Condition: We can employ this boundary condition when the simulation domain's electromagnetic fields and physical structures are periodic. Depending on periodicity and design configuration, we can apply this condition in one or two axes. This boundary condition based on structural and electromagnetic periodicity 'connects' the two ends of the simulation region. This boundary condition is symmetric. It means that this condition applies to both the positive and negative sides of the same axis, unlike other boundary conditions. For example, if the positive X side is periodic, the negative X side must be so.

Bloch Boundary Condition: This boundary condition is an extended version of the periodic boundary condition. We use it when there is a phase difference between fields involved in every unit cell. The most common use of this boundary condition is in the simulation of incident lights at an oblique angle.

Symmetric/Anti-Symmetric Boundary Condition: When a simulation setup has a plane of symmetry, we may utilize this boundary condition. The symmetric boundary condition serves as a mirror for the electric field, whereas it functions as an anti-mirror for the magnetic field. The anti-symmetric boundary condition serves as a mirror for the magnetic field and functions as an anti-mirror for the electric field.

The PML and Periodic types of boundary conditions are used in this thesis, as shown in Figure 3.1. We use the periodic boundary condition on the surfaces of the unit cell that are perpendicular to the x and y axes since the absorber structure is periodic in x and y directions with an unlimited extent.

3.1.3. Excitation and Spectra:

The simulation begins by creating a temporal pulse excitation using a plane wave source to generate a correct pulse spectrum, that is, a broad spectrum source. The planned time-domain pulse is then gets launched into the simulation domain. Because the simulation domain is periodic in both the x and y dimensions, the source geometry must be as well. We employed a variety of pulses with comparable but distinct spectra throughout our research. As a result, we describe the final and most generally utilized pulse below.

In our desired wavelength domain, we create a Gaussian spectrum in the frequency domain using a pulse with a starting offset of ~10 fs and a pulse duration of ~4 fs. We built the pulse to span our target range in the wavelength domain. The range is selected based on interest, numerical considerations, and the materials' data.

3.2. Fabrication

This thesis used Physical Vapor Deposition (PVD) and Chemical Vapor Deposition (CVD) techniques to fabricate the design. Specifically, we used two main pieces of equipment: i) thermal evaporation and ii) atomic layer deposition (ALD). This section provides detailed information on the operation principle of these techniques.

3.2.1. Thermal Evaporation

We can categorize deposition systems into two categories: 1) chemical vapor deposition (CVD) and 2) physical vapor deposition (PVD). In the PVD process, we deposit the target film physically on the sample, and there is no significant chemical interaction between the substrate and the film. However, we utilize a precursor gas in the CVD technique that evenly coats the substrate

host. A thermal evaporator is one of the most commonly used PVD tools. We heat the bulk rock of the deposition material (source) to temperatures about 1000 °C in this deposition equipment, which transforms the bulk rock into a molten liquid.

The machine sends a high electric current through the boat (usually made of very high melting temperature material such as molybdenum or tungsten) containing source material pellets. The liquid source material eventually evaporates in a vacuum environment, and vapor ascends toward the sample, which is on top of the source. In the thermal evaporator technique, the source is usually at the bottom of the chamber, while the target is at the top. The distance between these two components is around 80 cm in our equipment to ensure that the evaporation beams approach the target in a nearly uniform pattern. Furthermore, a rotating mechanism ensures that the sample surface has the same averaged evaporation rate. Specifically, in our samples, the uniformity of the coating is quite good because the samples are as small as 1 cm x 1 cm. The thermal evaporation tool employed in our depositions is in figure 3.2. Thermal evaporation occurs in high vacuum levels. The quantity of gas molecules within the chamber becomes negligible when the chamber pressure falls below a specific threshold, generally about $10^{-6}\ mTorr$. As a result of the reduced scattering between the molecules, the evaporation beam (particles) propagates with minor loss, resulting in a lengthy mean free path of a few meters. The system employs two pumps to achieve high vacuum levels: a mechanical pump and a turbopump. The mechanical pump reduces the chamber pressure to 10 mTorr. A gate valve then isolates the mechanical pump, and a turbopump is activated to generate higher vacuum levels. The deposition rate (measured in angstrom per second Å/s) increases when evaporation begins. An acoustic sensor measures the rate of deposition. We can assume the source is a point source that evaporates the material isotropically for practical purposes. Therefore, we can express the deposition rate as:

$$\upsilon = \frac{R_{evp}}{4\pi N r^2} cos(\theta_i) \quad (3.1)$$

Figure 3.2 The utilized thermal evaporation system

where R_{evp} is the source material's evaporation rate in atoms per second, N is the source material's density, and r is the distance between the target and the source site. According to this formula, the deposition rate has a cosine distribution, with the thickest deposition in the central region of the sample positioned immediately above the source and lesser deposition thicknesses in the corners at the end. To alleviate the nonuniformity problem in the coating and safely assume source material vapor rays are parallel to each other at the

destination, we chose the distance r between the source and sample is as large as practically feasible.

The deposition pressure, during our process, is kept below $6 \times 10^{-6}\ mTorr$. We deposited metals and dielectric layers using a Tungsten (W) boat. We continuously controlled the power at the source so that the deposition rate stayed around $2\ \text{Å}/s$. Based on our practical experiences, higher deposition rates result in a rougher film surface, whereas lower deposition rates result in more nonuniform film thickness, meaning the center of the sample becomes thicker than the corners.

3.2.2. Atomic Layer Deposition

Another technique used in this thesis work is Atomic Layer Deposition (ALD). ALD is a CVD-based method where the source material for film deposition is chemicals in the gaseous phase. In this technique, the layer forms a chemical bond with the host substrate, and therefore, the film quality of this method is much better than PVD-based methods such as thermal evaporation. Moreover, ALD also has some advantages compared to other standard CVD methods such as low-pressure CVD (LPCVD) and plasma-enhanced CVD (PECVD), which is its low operation temperature (ranging between 80-300 ºC). During an ALD process, the source of each element, a gas form reactant, is sent into the chamber in a consecutive approach. In this method, multiple reactants do not get flowed into the chamber simultaneously, but instead, a sequential way is employed. At the end of every ALD cycle, a single atomic layer of the target material is grown. Each deposition cycle (each of the two needed) is self-terminating, where every cycle forms an angstrom thick layer at the end of the process.

Consequently, we can control the deposition rate precisely, and the final film has better homogeneity than the previously mentioned deposition methods. In addition, although researchers have widely used ALD in metal oxide and nitride depositions, volatile precursors for metal coatings also have recently

been discovered. Finally, we should emphasize that there is no requirement for an ultra-high vacuum in this process. Moderate vacuum levels are sufficient for an ALD process to happen. The utilized ALD system is in Figure 3.3.

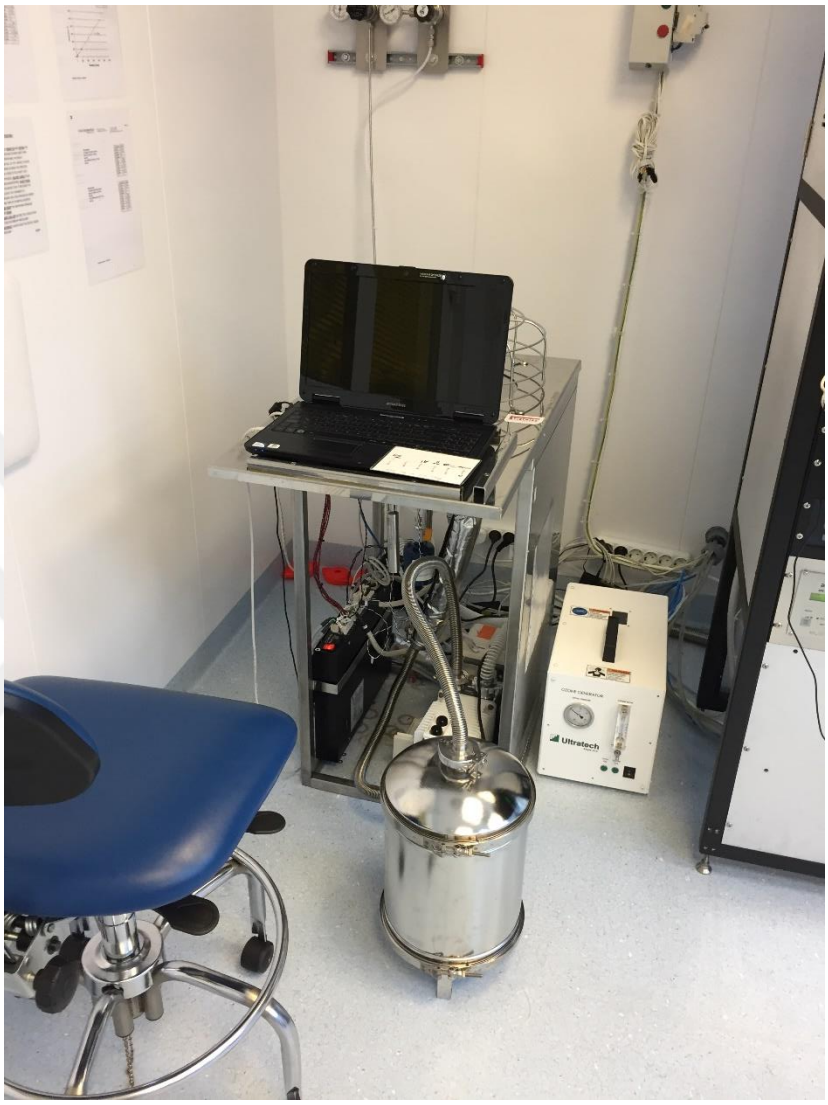

Figure 3.3 The utilized ALD system in the deposition of the Al_2O_3 layer.

3.2.2.1. ALD System Parts and Their Function

The ALD system comprises the following parts:

***Carrier Gas*:** N_2, an inert gas that does not react with chemicals and just delivers them to the chamber, is utilized as the carrier gas. When the deposition of a cycle is over, the carrier gas purges the reaction byproducts. We maintain

a steady supply of inert gas throughout the process, even in standby conditions. In the working pressure of about 1 Torr, we regulate the flow rate precisely for each process. In our depositions, we fixed the flow rate at 20 sccm value.

Sources and precursors: Inside metallic cylinder containers are gaseous chemical source materials. A microsecond valve is located at the end of each container and may open and close very fast during the pulsing process. This valve's minimum pulse time is 15 milliseconds. In our case, we used Trimethyl Aluminum (TMA) as Al precursor ($Al(CH_3)_3$). Moreover, we employed deionized (DI) water as the oxygen source.

Heaters*:* There are two planar and wire heaters in the chamber, one in the center and the other on the periphery. As a result, the heat is distributed evenly throughout the whole chamber. Two more heaters are wrapped around the pipelines in addition to the chamber heaters to keep the precursor gas temperature near to the chamber temperature. The minimum needed temperature is 80°C, and raising the temperature to higher values within a specific range helps speed up the deposition process. There is a possibility of precursor breakdown and undesired chemical reactions at very high temperatures, such as above 300 °C. For this study, we kept the chamber temperature at 200 °C, while the pipe temperatures were at 150 °C.

***Reaction Chamber and Exhaust System*:** The chemical reaction necessary for deposition occurs in the reaction chamber. This chamber has one gas input for allowing precursors and one gas output to remove leftover gasses. The chamber is kept at moderate pressure levels using a vacuum pump.

3.2.2.2. ALD Operation Principle

The ALD process is a self-terminating one in which consecutive pulsing of various metal and oxygen-containing precursor gases leads to producing a monolayer metal oxide, as described in previous sections. In the case of this thesis work, we employed a carrier gas flow of 20 sccm and a pulse duration of 15 ms for both Al and O precursors. Both precursors are pulsed into the

chamber and then purged for 20 seconds once the temperature stabilization occurs at 200 °C. Water is chemically adsorbed on the surface as OH agents in this deposition technique.

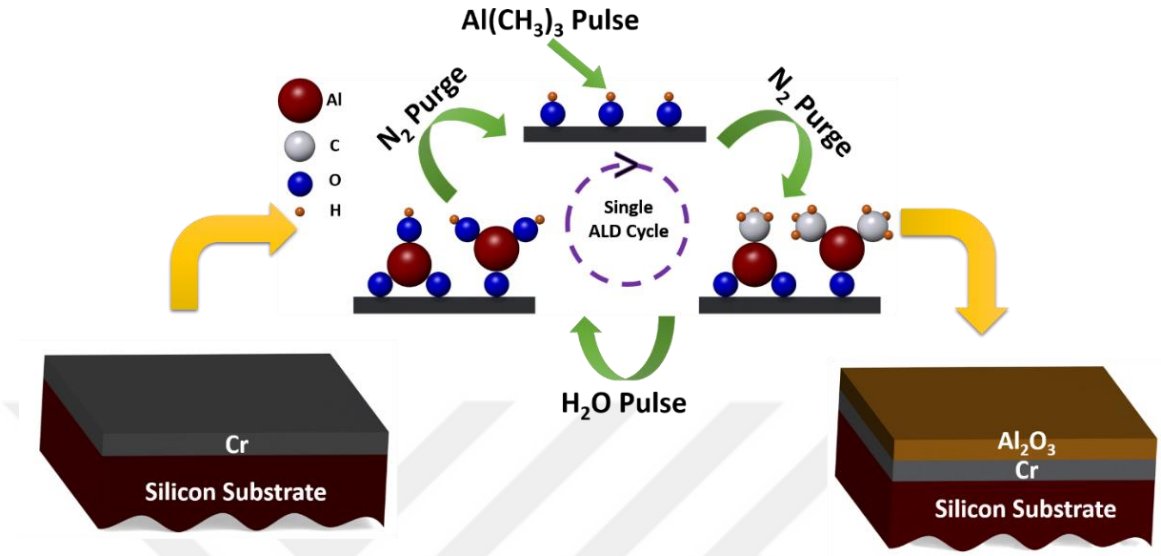

Figure 3.4. The schematic representation of ALD deposition of Al_2O_3 layer[7].

Then in the second half of the cycle, the TMA is introduced into the deposition environment in similar pulse and purge time constants. The H molecule detaches from the surface during this process, and Al forms a chemical bond with the surface instead. With the bonding of Al to the O surface, Al_2O_3 formation is complete. We explained this schematically in Figure 3.4. The chemical reaction of the process is as follows:

$$3H_2O + 2Al(CH_3)_3 \rightarrow Al_2O_3 + 6CH_4 \quad (3.2)$$

3.3. Characterizations

This section presents a brief discussion on the operation mechanisms of used equipment for the characterization, along with the measurement results. Then, we present the characterization tools used in this thesis work. In our characterization process, we used the ellipsometry tool to measure and extract

the permittivity and thickness of every layer. Then we used transmission electron microscopy (TEM), scanning electron microscopy (SEM), and atomic force microscopy (AFM) to examine the fabricated sample structurally. Next, we used Fourier Transform Infrared Spectroscopy (FTIR) spectroscopy to characterize the absorption response of the device optically. Finally, photoluminescence spectroscopy and imaging are employed to examine the emission property of the light-emitting materials.

3.3.1. Ellipsometry

An ellipsometer is a device that can characterize a thin film sample's thickness and refractive index. The Ellipsometer illuminates the sample with a polarized beam, which then reflects off the sample's surface. Then a rotating polarization-sensitive detector measures the reflected beam. Thus the polarization change on the reflected beam can be observed at each illumination angle, and measured data is fit to a model. Figure 3.5 shows the ellipsometry system that we used in our characterizations. Some of the characterizations of individual materials were conducted even before the metamaterial design process, specifically to provide the design process with accurate data. For example, we characterized the Ge and Ni layers used in one of our designs by ellipsometry before the actual device fabrication. For this aim, we put the sample in the V-VASE ellipsometry equipment and applied the angled measurement on the sample for five different incident angles of 55°, 60°, 65°, and 70°. After performing this spectroscopic measurement, we fit the obtained data to extract the permittivity data of each layer.

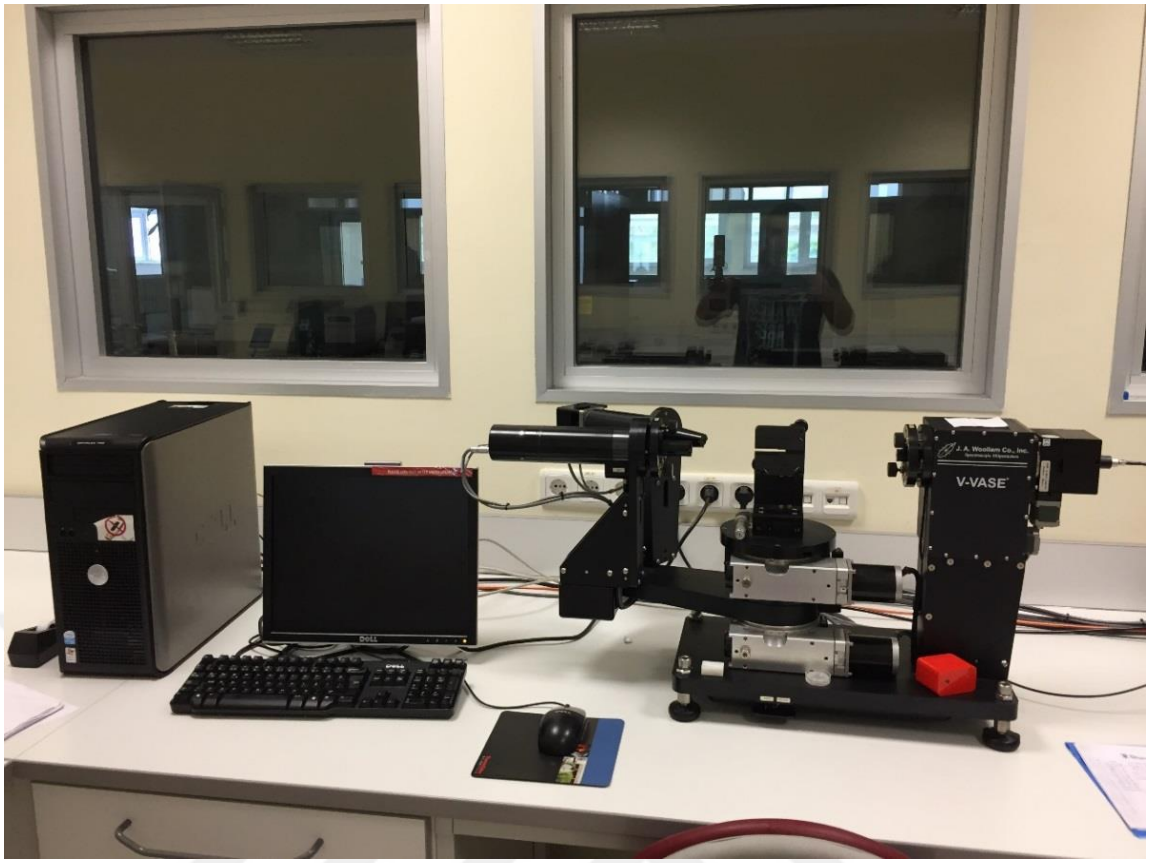

Figure 3.5. The ellipsometry system we used in our characterizations.

3.3.2. Scanning Electron Microscopy

Scanning Electron Microscopy (SEM) employs accelerated electrons to image a sample, much like any other electron microscopy approach. In an SEM system, as shown in Figure 3.6, an electron beam images the surface by collecting the reflected (backscattered) and secondary electrons by a detector. The picture resolution is substantially greater because accelerated electrons have a shorter (De Broglie) wavelength than optical photons. An SEM picture can have a resolution of up to 5 nanometers. However, the sample we image must be within a vacuum chamber in SEM. Vacuum is necessary because the electron source is a highly delicate component that must always be kept in a vacuum; otherwise, it deteriorates. And the procedure would be rendered worthless if free electrons collided with gaseous molecules within the chamber.

Figure 3.6. SEM system we used in our characterizations.

3.3.3. Fourier Transform Infrared Spectroscopy

The FTIR technique is an indirect interferometric measuring technique that can be employed to obtain a broad spectrum response in the visible, near-infrared (NIR), mid-infrared (MIR), and far-infrared (FIR) domains. In addition, the capacity of the setup to gather all wavelengths concurrently contributes to the speed of FTIR measurements. Using an interferometer, we first acquire an interferogram of the signal. We then obtain the spectrum by performing a Fourier transform on the interferogram. Finally, we collect the interferogram data digitally and compute the Fourier transform using an FTIR setup. The approach works well in the infrared regime, as its name implies, and is notably beneficial owing to the high signal-to-noise ratio that can be achieved with excellent spectral resolution and precision. The system is depicted in Figure 3.7.

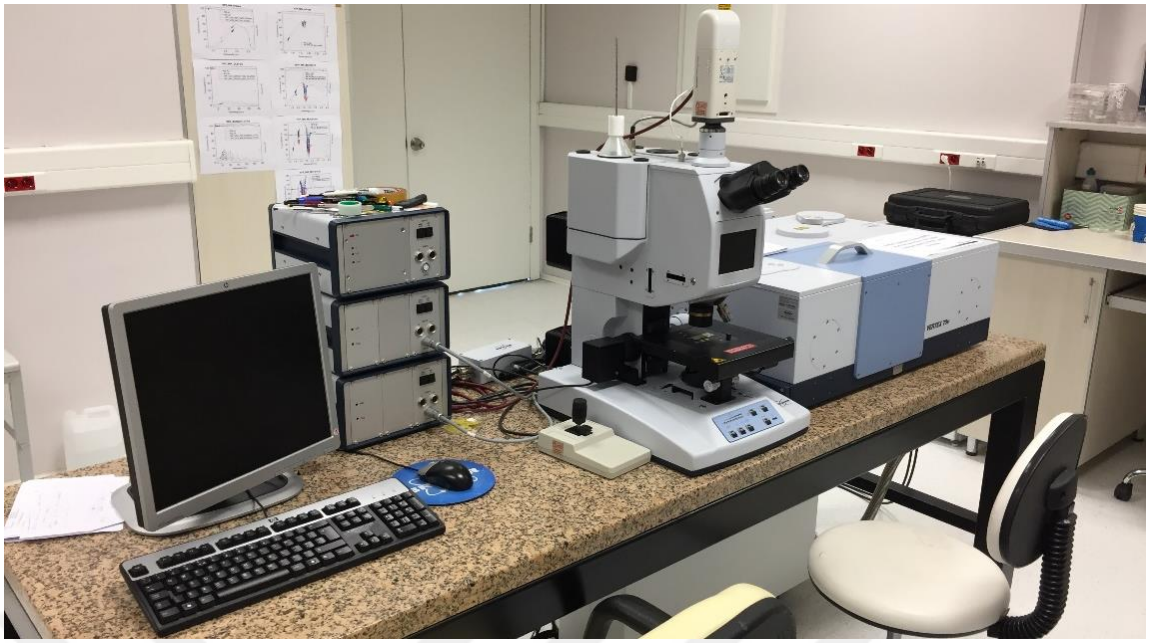

Figure 3.7. The FTIR system we used in our measurements.

3.3.4. Photoluminescence Spectroscopy

Fluorescence or photoluminescence (PL) spectroscopy is a valuable technique to investigate the material properties and dynamics taking place at the nanoscale due to the high sensitivity of the photo-physical properties of the materials to even small changes at the molecular level. PL is the spontaneous emission of light from the material under optical excitation. The main principle of operation of photoluminescence spectroscopy relies on spectrally selective excitation of the samples and spectrally analyzing the emission signal. PL analysis is non-destructive. When we excite a sample with a stream of photons having energies higher than the semiconductor (SC) bandgap, electrons are detached from holes and are excited to the SC's conduction band (CB). These excited electrons are relaxed through the recombination with their counterparts at the valence band (VB). This relaxation can be radiative or non-radiative. If it becomes radiative, it shows itself as an emitted light.

We can attribute the spectral distribution of PL data to different factors, including the bandgap and the defect states' energetic position. If the PL peak originates from CB to VB transition, it is called band-to-band emission. We can

use peak position to estimate the E_g of SCs. This transition may also occur through a trap state. A trap state can be anywhere inside the bandgap of the SC. Photons emitting from a trap state's radiative recombination have lower energy than band-to-band ones. We can attribute the spectral position of these sub-peaks to the energetic location of trap states.

Moreover, we can use the intensity of this data as a measure to estimate the electron-hole pair separation in a heterojunction design. Upon illumination, the excited electrons transfer from the CB of material into that of other material, and via this separation, their radiative recombination probability decreases. Thus, quenching in PL intensity can be interpreted as the electron-hole pair separation.

CHAPTER 4. GENERATION OF ADDITIVE COLORS WITH NEAR-UNITY AMPLITUDE USING MULTILAYER TANDEM FABRY–PEROT CAVITY

4.1. Preface

This chapter of the thesis is based on the publication "*Generation of additive colors with near-unity amplitude using a multilayer tandem Fabry–Perot cavity*," A. C. Kosger, A. Ghobadi, A. R. Rashed, H. Caglayan, and E. Ozbay, Optics Letters. **46**, 3464 (2021). Adapted (or "Reproduced in part") with permission from Optica Publishing Group, Ref[114].

4.2. Introduction

Inspired by natural photonic designs, such as Morpho butterfly, structural coloring based on nanophotonics and nanoplasmonics designs has been the subject of many studies in recent years[115]. In an ideal scheme, a color filter selectively transmits/reflects/absorbs a narrow wavelength range while having a weak light-matter interaction in non-resonant regions. Scientists have utilized various design architectures to fabricate color filters in reflection and transmission modes. Designs operating based on surface plasmon resonance[116]–[120], guided-mode resonance[121]–[125], and photonic crystals[126], [127] as well as other innovative ideas [128], [129] are some of these approaches. However, they accomplish color generation in all of these designs via spectrally selective light-matter interaction in sub-wavelength metal/dielectric nano units. However, the realization of these nano units requires complex fabrication routes, such as electron-beam lithography (EBL) and nano-imprint lithography (NIL) that are large-scale incompatible approaches. Therefore, lithography-free design structures have attracted much attention in recent years[130].

Among all the resonators, metal-insulator (MI) pair based Fabry-Perot (FP) resonators are the most commonly employed designs for a large-scale

color generation[77]–[80], [83], [85], [86], [131], [132]. These multilayer designs provide strong interference in spectrally selective regions. Generally, these planar designs produce additive red-green-blue (RGB) colors in transmission mode and subtractive cyan-magenta-yellow (CMY) colors in reflection mode. Unlike reflection mode designs that can reach near-unity amplitude, transmissive RGB colors have efficiencies lower than ~0.7 due to multiple lossy layers in their propagation path. A possible solution to tackle this deficiency is proposing a planar lithography-free architecture to generate RGB colors in the reflection mode. Previous researchers proposed the use of lossy metals such as bismuth[133] and nickel [134] as the top layer in a metal-insulator-metal (MIM) design to achieve this goal. However, these designs' wide full-width-at-half-maximum (FWHM) values reduce color purity. Other researchers explored innovative architectures to generate RGB colors in reflection mode, but their efficiency was also below unity[135], [136].

This work demonstrates the generation of RGB colors numerically and experimentally using a designed metal-dielectric medium. For this, first, a modeling approach based on the transfer matrix method (TMM) is developed to compare the performance of common MIM cavities with those of metal-insulator-metal-insulator (MIMI) ones. Later, using numerical simulations, the optimal geometries are extracted. Then, based on the results of numerical simulations, a hybrid structure made of metal-insulator-metal-semiconductor-insulator (MIMSI) stacks is optimized to create RGB colors with high purity and near-unity amplitude. Finally, we utilize the optimal geometries to fabricate RGB color filters with an amplitude >0.9 reflection peak and FWHM $<0.3\lambda_{peak}$. The findings of this study show that a proper connection of cavities in a tandem scheme can offer diverse functionalities that cannot be realized with single FP resonators.

4.3. Numerical Simulations

We scrutinize the reflection characteristics of two typical FP resonators of MIM and MIMI using a modeling approach explained in the second chapter, see

Figures 4.1(a-f). Our group's previous studies have also explained the details of this modeling [33]. In this modeling, the bottom layer is an optically thick aluminum mirror, the spacer thickness (D_I) is 60 nm Al_2O_3 layer, and we extract the reflection contour plots for different top metal thicknesses (D_M) of 5 and 15 nm. We obtain these contour plots for five different wavelength values of 450 nm, 500 nm, 550 nm, 600 nm, and 650 nm. In these 2D plots, the centric blue semi-circles show the real and imaginary permittivity values required to have <0.1 reflections (absorption >0.9). When we compare these results, we understand that the tolerable region for perfect light absorption is more comprehensive for the MIMI design (compared to that of MIM). Moreover, thicker D_M values lead to wider perfect absorption circles. In addition, these circles are in the vicinity of the center, and a lossy metal with real and imaginary parts close to zero provides better performance than the alternative. Therefore, from these modeling findings, in a MIMI absorber made of a lossy metal, constructive interference at a specific wavelength leads to near unity reflection, while the other parts of the spectrum are perfectly absorbed. In this way, we can generate an RGB color filter, in the reflective mode, with high efficiency and color purity.

To verify these modeling outputs and find the optimal geometries of the RGB color filter, the numerical simulations, using the Lumerical finite-difference-time-domain (FDTD) software package, are performed[137]. In the FDTD simulations, we illuminated the unit cell with a broadband plane wave at normal incidence. We chose the bottom layer as a 150 nm thick Al layer in the simulations. We set the insulator layers as Al_2O_3 with identical thicknesses of D_I.

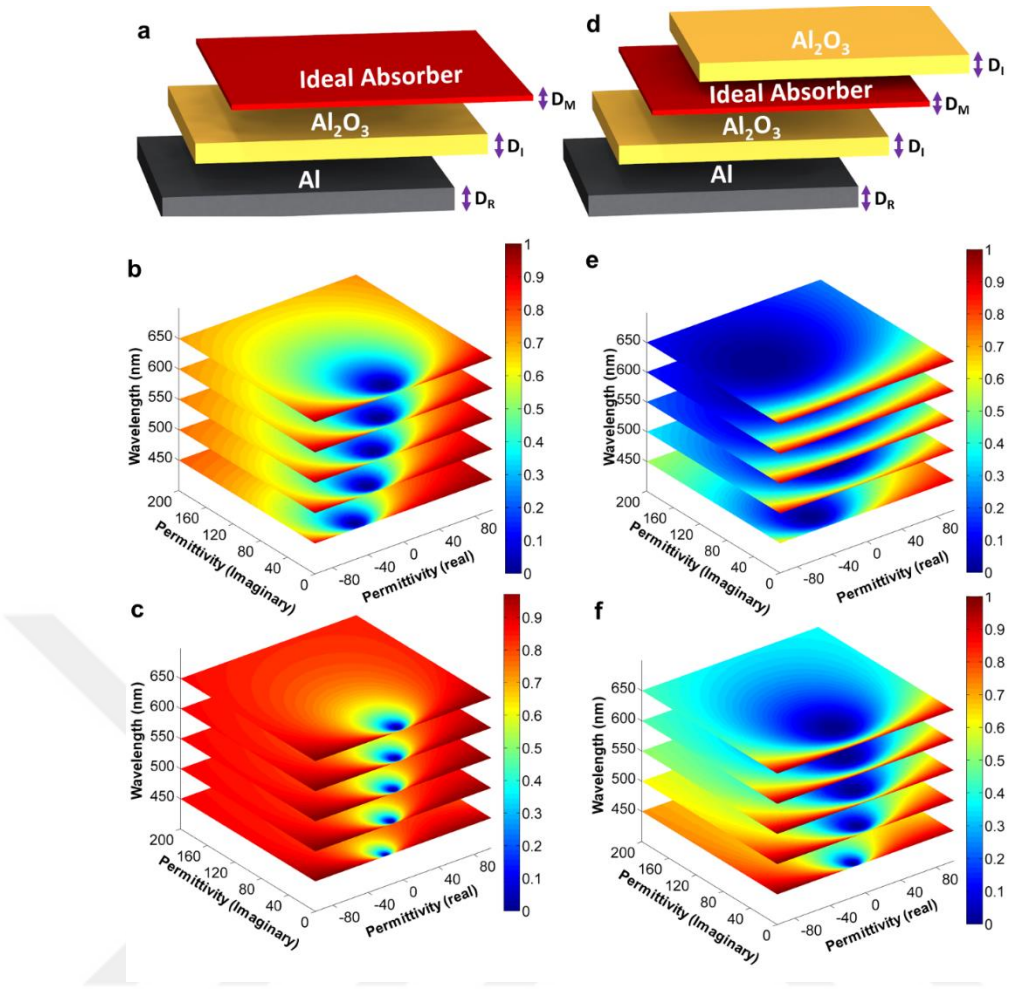

Figure 4.1 Schematic representation of (a) MIM cavity design. The reflection contour plots of an MIM cavity at different real and imaginary permittivity values for D_M of (b) 5 nm and (c) 15 nm. Schematic representation of (d) MIMI cavity design. The reflection contour plots of an MIM cavity at different real and imaginary permittivity values for D_M of (e) 5 nm and (f) 15 nm. In all of the modeling results, we set the (DI) as the 60 nm Al2O3 layer, and the bottom layer is an optically thick Al layer. The color bar shows the reflection value of the cavity.

Finally, the top metal layer is Ni with a thickness of D_M. All the permittivity data are from the Palik model[138]. In this design, two primary geometries of D_I and D_M are responsible for the optical behavior of the cavities. Therefore, we separately studied the impact of these two factors for both MIM and MIMI cavities. First, we fixed the insulator layer thickness and then swept the metal layer thickness to find the optimal value for perfect light absorption.

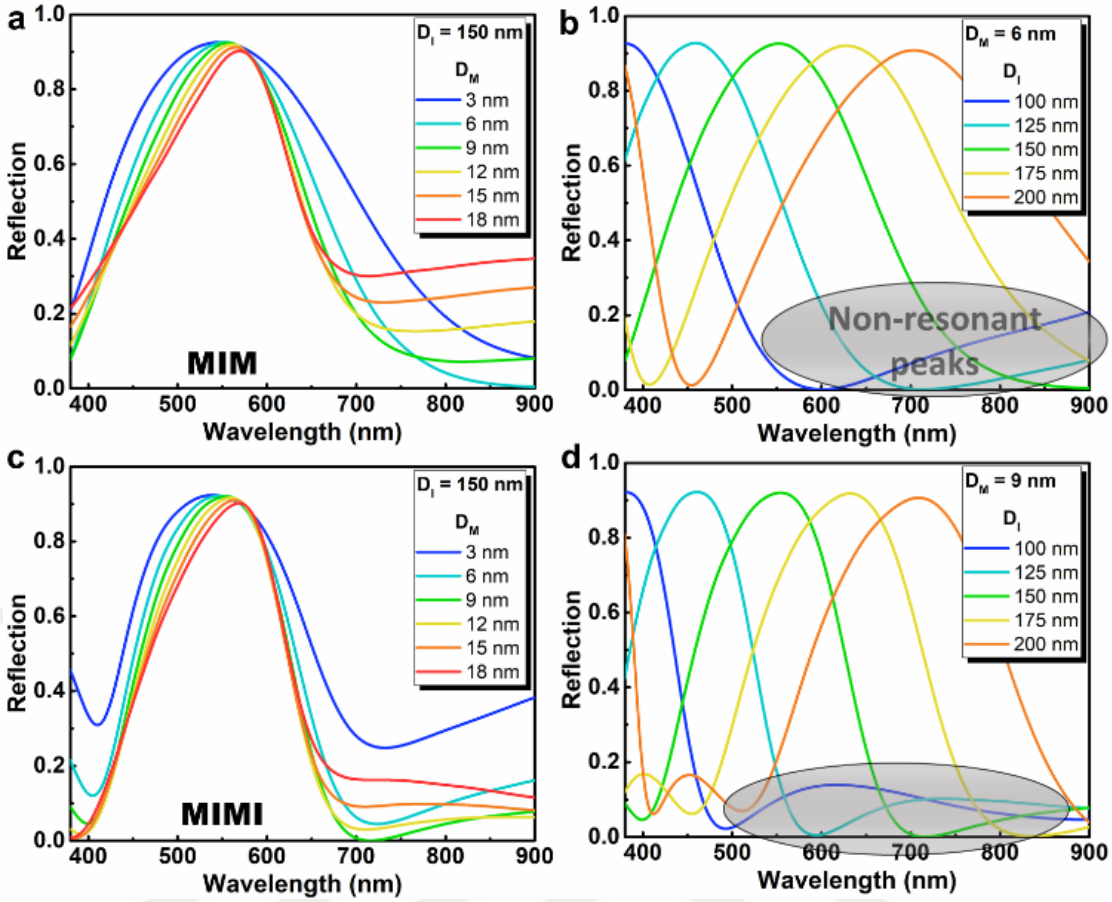

Figure 4.2 The reflection spectra of MIM cavity design for different (a) D_M and (b) D_I values. The reflection spectra of MIMI design for different (a) D_M and (b) D_I values. The highlighted regions show the non-resonant ripples.

Later, we fix the metal layer thickness at the optimum value, and the spectral shift of this resonance peak in different insulator layer thicknesses is studied. As shown in Figure 4.2(a), for MIM design, D_I is fixed at 150 nm, and D_M is swept from 3 nm to 18 nm, with a step of 5 nm. As this panel implies, the reflection peak amplitude is almost constant for all metal thicknesses. However, as we go toward thicker layers, the FWHM gets narrower. However, at the expense of this narrowing, the non-resonant response (reflection ripples in the non-resonant spectral range) becomes more prominent and this, in turn, reduces the color purity of the filter. Therefore, we can provide a suitable trade-off between these two factors in an appropriate metal thickness layer. This trade-off is satisfied in $D_M = 6$nm for the MIM cavity absorber. Setting this as the top layer, we swept D_I from 100 nm to 200 nm (with 25 nm step). From

Figure 4.2(b), the reflection peak is monolithically shifted from blue to red wavelengths, without any loss in its amplitude. However, blue filters (lower wavelength ranges) suffer from non-resonant absorptions (in the more extended visible range), leading to poorer color pureness. A similar analysis is performed on an MIMI cavity absorber, as shown in Figures 4.2(c)-(d). For MIMI color filters, the optimal D_M is 9 nm. Compared with MIM cases, MIMI designs have smaller FWHM but are similar to the MIM case, and they also have non-resonant absorption ripples and, therefore, low color vividness.

The above findings show that the MIMI configuration based color filters perform better in RGB color generation than MIM ones. However, both designs have poor color purity, and it seems that we cannot achieve good color purity using a conventional single cavity FP resonator. Therefore, the simultaneous realization of color purity and efficiency needs a tandem scheme FP design. Back to the modeling data proposed in Figure 4.1(f), to have near-zero reflection in all wavelength values, we need to approach the effective permittivity of the metal layer to the zero centers. In other words, instead of a single metal, we can use an effective metal-dielectric double-layer to reduce the effective permittivity values toward lower ones. For this purpose, a multilayer design based on metal-insulator-metal-semiconductor-insulator (MIMSI) stacks is developed, as seen in Figure 4.3(a). The semiconductor layer is Ge with a thickness of 3 nm while keeping all other geometries are at the optimal values of the MIMI structure. We compare the reflection spectra of MIMI and MIMSI designs in Figure 4.3(b). As this figure depicts, the addition of an ultrathin Ge layer lowered the FWHM of the reflection peak and effectively mitigated the non-resonant absorption ripples. The absorbed power across the MIMI and MIMSI cavities are in Figures 4.3(c)-(d) to understand the function of this Ge layer on the overall optical performance of the MIMSI FP cavity. We should mention that, in these contour plots, the profile focused on the active middle layer, and this data belongs to the case of the red filter. From these panels, the Ge layer harnessed most of the incoming power in the shorter λ values, and Ni is the active material in the longer ranges, while both of these layers are transparent in the peak resonance position. This phenomenon can

be seen from the linear plots as well (Figure 4.3(b)), where the sub-peaks (non-resonant modes) in the reflection of MIMI do not occur in the MIMSI design. Therefore, using this designed FP resonator, it is possible to achieve large-scale compatible and high-efficiency RGB vivid colors in the reflection mode color filters.

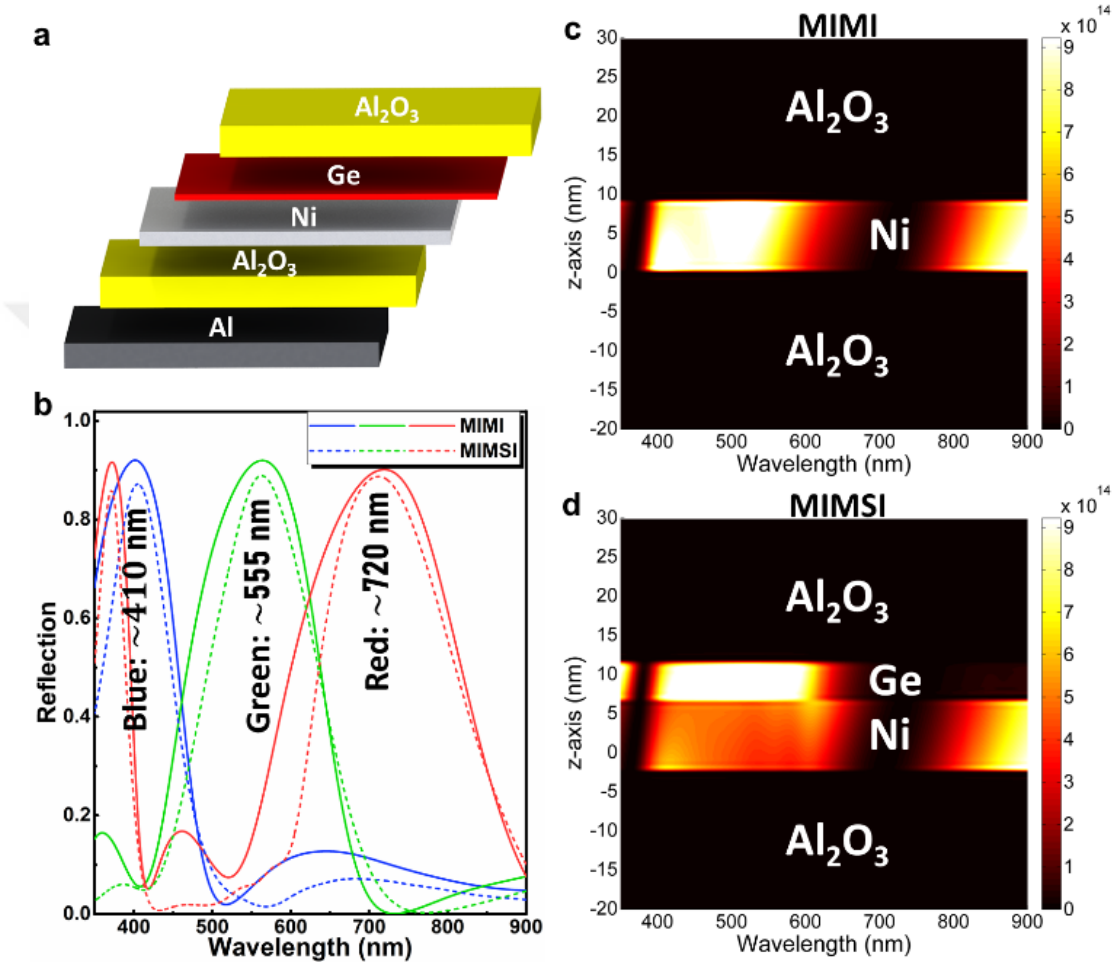

Figure 4.3 (a) The schematic representation of MIMSI cavity design, (b) the reflection spectra of RGB color filters for MIMI and MIMSI structures, the absorption profile across the cavity structure for (c) MIMI and (d) MIMSI color filters. The color bar shows the absorbed power value.

4.4. Results and Discussions

The Gaining insight into the design operation of the proposed MIMSI FP cavity and optimizing its performance using numerical simulations, in the next

step, this simulation data has to be verified by experimental data. For this aim, we fabricated a set of MIMSI samples with optimized D_M values of 9 nm and different D_I thicknesses (from 110 nm to 200 nm by a step of 15 nm) using cleanroom facilities. A similar set is fabricated for MIM architecture to better compare qualitatively with a typical FP color filter. We diced the Si wafer into 1 cm × 1 cm pieces for the fabrication, applying a standard cleaning process. The metallic (both Al and Ni) and Ge layers are coated at the desired thicknesses, using the thermal evaporation technique. We set the deposition rate at around 1.5-2 A°/s for all layers, and we kept the chamber pressure below 5e-6 Torr throughout the deposition process. For Al_2O_3 coating, atomic layer deposition (Cambridge Nanotech Savannah S100) is used at 250°C using $Al(CH_3)_3$ and water precursors as aluminum and oxygen sources. We chose the pulse and purge times to be 0.015 s and 10 s. The optical image of fabricated MIM and MIMSI samples is present in Figure 4.4(a). We can deduce that MIMSI cavities have better color vividness than MIM ones from their visual appearance. We utilized Scanning electron microscopy (SEM) imaging to verify the formation of different layers. Cross-sectional SEM images of the MIM and MIMSI samples, shown in Figures 4.4(b-c), confirm the successful growth of all layers. After the initial structural analysis, we utilized optical characterizations to probe the reflection response of each sample. To measure the normal incidence reflection, in the wavelength range of 0.4–0.9 μm, we used an in-house setup comprising a halogen lamp as the incident light source, where this source was integrated into a microscope to collect the reflected light from the surface. Figure 4.4(d) shows that the MIM color filter has reflection peaks above 0.95. This peak value gradually reduces, but it stays above 0.9 for MIMSI cavity designs, as seen in Figure 4.4(e).

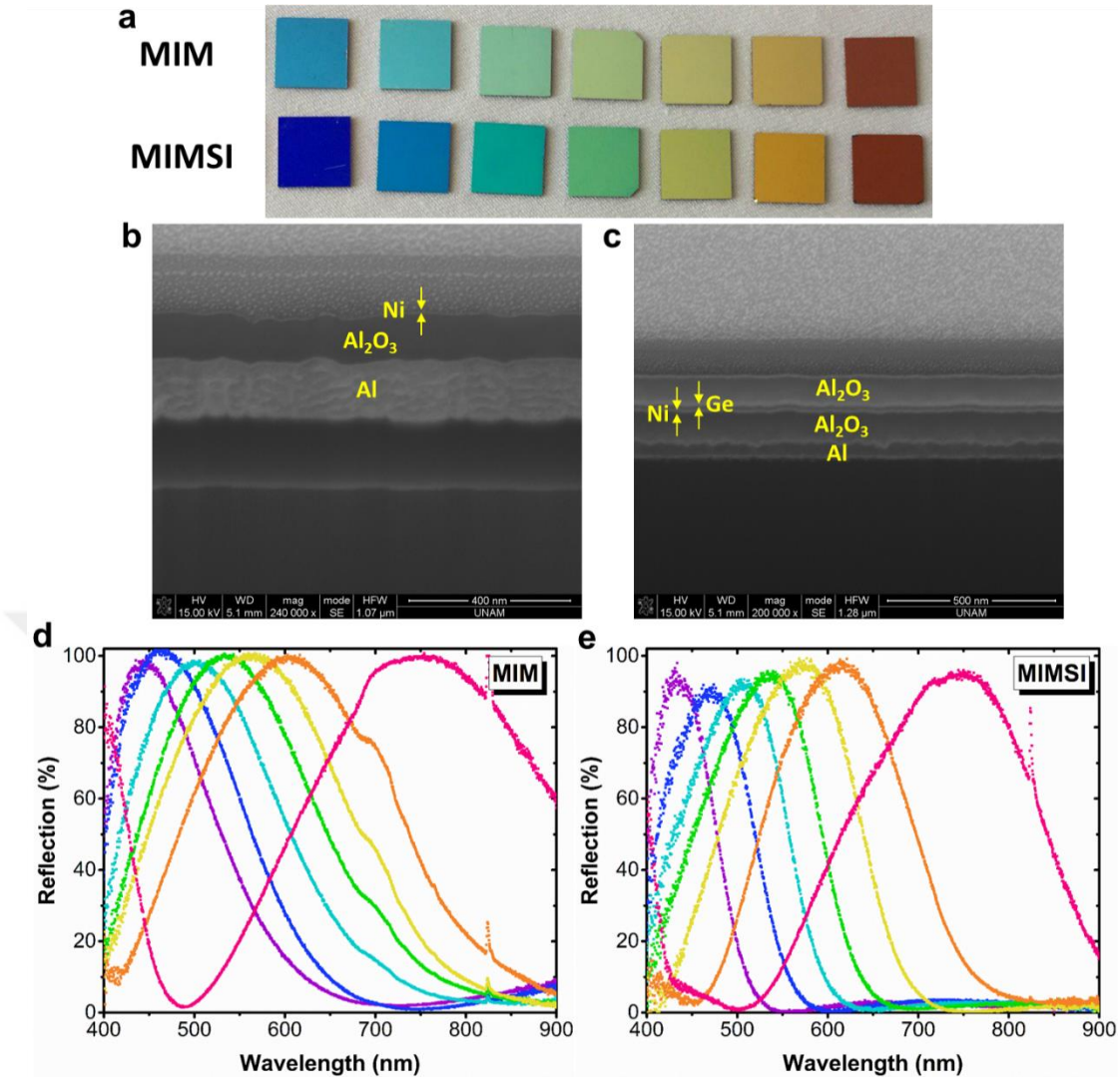

Figure 4.4 (a) The optical image of MIM and MIMSI samples with different spacer thicknesses generates RGB colors. The cross-sectional SEM image of the (b) MIM and (c) MIMSI cavity designs. The measured reflection spectra of different (d) MIM and (e) MIMSI samples.

However, in a one-by-one comparison, it can be found that MIMSI designs have considerably lower FWHMs and relatively small non-resonance reflection colors. For instance, in the case of the blue color filter (for D_I =110 nm), the FWHM for MIM and MIMSI samples are 131 nm ($0.3\lambda_{peak}$) and 77 nm ($0.17\lambda_{peak}$), respectively. On the other hand, these values for green color (D_I =155 nm) are 231 nm ($0.43\lambda_{peak}$), and 141nm ($0.26\lambda_{peak}$) and red color (D_I =200

nm) are 323 nm ($0.43\lambda_{peak}$), and 228 nm ($0.3\lambda_{peak}$), for MIM and MIMSI samples, respectively.

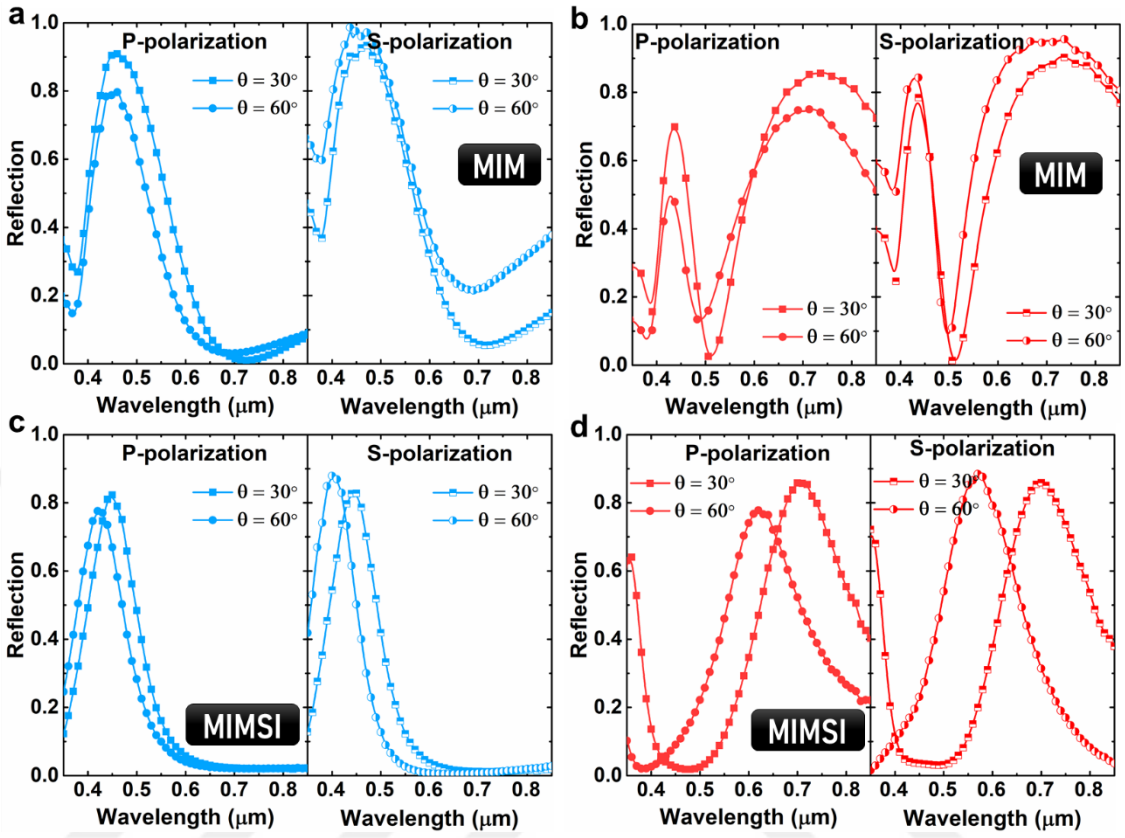

Figure 4.5 The angular response of the MIM filter for two different colors of (a) blue and (b) red. The angular response of the MIMSI structure for two different colors of (c) blue and (d) red. We carried out the measurements at both p and s polarizations and two different incident angles of 30° and 60°.

We should consider that another factor in the performance analysis of these FP filters is their angular response. For this aim, ellipsometry measurements are carried out in two incidence angles of 30º and 60º at S and P polarizations for both MIM and MIMSI designs with blue and red color filters, see Figures 4.5(a)-(d). As these panels imply, overall, the resonance wavelength is shifted toward the blue region in both cases. These shifts are more pronounced in the MIMSI designs than in the MIM designs due to the longer optical path of light in these samples (compared to MIM ones). However, the color purity (peak shape and non-resonant response) is significantly modified in the MIM designs, while

MIMSIs have kept their peak shape and FWHM width almost intact. This result is because the top insulator layer in a MIMSI structure acts as a broadband anti-reflective coating that provides phase-matching conditions in a broad wavelength and incident angles.

4.5. Summary

In summary, this work demonstrates the effectiveness of tandem shape FP designs in achieving optical behaviors that cannot be realized with standard cavity designs. Furthermore, the high efficiency and color purity of these planar MIMSI designs, together with their large-scale compatibility, bring them the opportunity to be scaled up for commercial applications.

CHAPTER 5. DISORDERED PLASMONIC NANOCAVITY ENHANCED QUANTUM DOT EMISSION

5.1. Introduction

Plasmon–exciton interaction in hybrid nano designs can efficiently amplify the fluorescent intensity of quantum dot (QD) emitters, going far beyond the single emitter limits [139]. The excitation of localized surface plasmon resonances (LSPRs) in a nanometal unit could effectively tailor the QD emitter's characteristics [140]–[145]. The large wave-vectors of surface plasmons trigger the confinement of EM fields into dimensions much smaller than the wavelength, and these local hot spots provide the opportunity to achieve strong light-matter interaction in QD units. The field confinement in these hot spots increases the density of excited electron-hole pairs, consequently intensifying their photoluminescence (PL). Along with excitation enhancement, the Purcell effect also comes into play when a QD emitter is near a plasmonic structure[146]–[149]. The Purcell effect leads to accelerated radiative recombination of QD excitons. Although placing QD emitters within these hot spots (formed in nanosized gap regions) can significantly enhance the spontaneous emission (SE) rates of quantum emitters [150]–[152], the story is quite different for a single isolated metal particle. The proximity (or direct contact) between a plasmonic antenna and a QD emitter can cause PL quenching through the nonradiative recombination of the excited pairs [153]–[155]. In other words, the provided solution should work for near touching and isolated plasmonic units. We can effectively suppress the non-radiative recombination by placing a nano spacer between the emitter and the plasmonic antenna. Nano spacer placement is the case for many designs where authors use polymer-QD dispersion and spin-coat the film onto the plasmonic substrate. However, the near field confinement in plasmonic units is effective in the vicinity of plasmonic units. This enhancement decays as we move away from plasmonic units. Therefore, the dispersion of QD emitters inside the polymer bulk effectively reduces the plasmon-exciton interaction. In an ideal scenario,

the plasmonic antenna should be isolated from the QD emitter to suppress the quenching phenomenon while staying close enough to be efficiently coupled with plasmonic hot spots. Moreover, the ideal near touching plasmonic design should have a feasible fabrication route with the potential for production at scale [130].

The weak coupling between QDs and plasmonic cavities leads to the Purcell Effect coming into play. The Purcell enhancement factor is:

$$F_P = \frac{\gamma_{cavity}}{\gamma_{free\ space}} \propto Q\left(\frac{\lambda^3}{V_{eff}}\right)$$

Low Q values, due to the ohmic losses, of plasmonic nanocavities compensated by minimal V_{eff} volumes. Low Q values also allow faster emission of photons from the cavity. Therefore substantial enhancement of spontaneous emission can be expected from QSs near plasmonic nanocavities.

In this chapter, we design and fabricate a plasmonic nanocavity design to maximize the PL enhancement in a QD-plasmonic hybrid design. The proposed design comprises disordered, tightly packed Au nanoislands with thin aluminum oxide (Al_2O_3) spacer layer. The resultant design has multiple sizes ranging from wavelength-scale to deep sub-wavelength geometries. In large nanoislands and isolated small units, the Fabry-Perot (FP) resonance in the formed MIS cavity is a dominant process to enhance the PL emission of the QDs. However, the main ruling factor in PL intensification in nano-sized gap regions is the coupling of plasmonic hot spots into QD emitters, i.e., excitation enhancement, along with the Purcell effect. We found that, in an optimal insulator thickness of 20 nm, we have both FP and hot spot formation effectively, leading to a PL amplification as significant as eightfold compared to a single QD design.

5.2. Numerical Simulations

At first, we studied the impact of nanocavity design in the light-matter interaction of a QD assembly using numerical simulations in the Lumerical finite-difference-time-domain (FDTD) software package [137]. To simplify the picture, we model the self-assembled QDs with a continuous thin film with a thickness equal to the particle's size (see Figure 5.1(a). Then, we studied the impact of an MIS cavity formation (Figure 5.1(b)) on the absorption characteristics of the CdSe film.

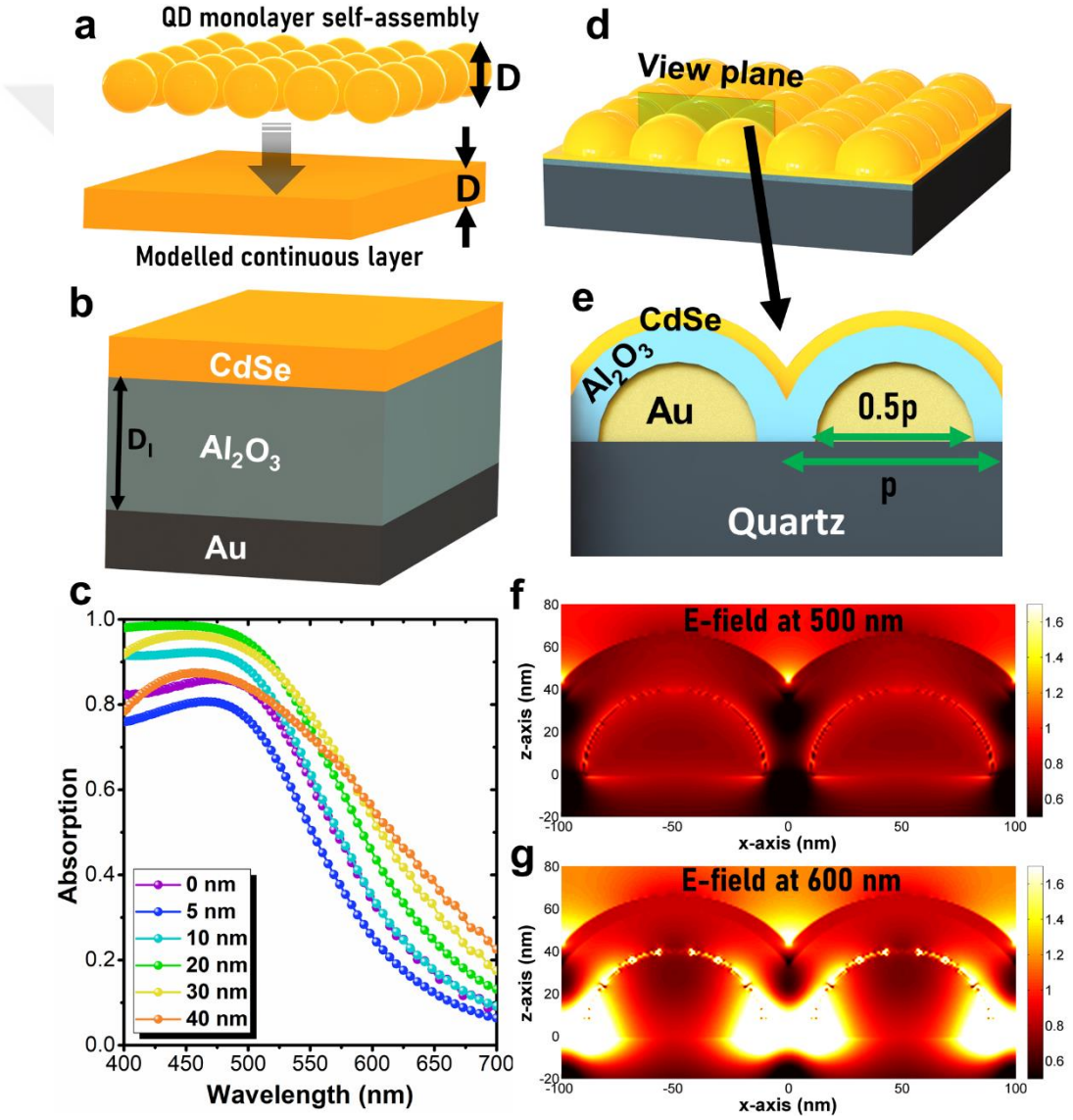

Figure 5.1 Schematic representation of (a) a self-assembled QD layer and its continuous layer model, (b) the MIS cavity design, and (c) simulated absorption spectra for different spacer thicknesses. (d) The simulated plasmonic design and (e) its cross-sectional view. The electric field enhancement in the view plane for two different wavelengths of (f) 500 nm and (g) 600 nm.

Considering the fact that the experimentally used particles are 6 nm in diameter, we fixed the top layer thickness at this value and investigated the impact of the spacer layer thickness on the absorption response of the cavity. We chose the thickness of the bottom layer as an optically thick Au layer with no transmission in our desired range. Therefore, we calculated the absorption (A) as A=1-R, where R is the reflection spectrum of the design. The absorption response of nanocavity design for different insulator thicknesses (D_Is) is in Figure 5.1(c). The formation of Fabry-Perot (FP) resonance modes leads to near-perfect absorption in short-wavelength ranges (400 nm-525 nm). As this panel implies, at a 20 nm insulator thickness, the substantial interference leads to near unity absorption efficiency. Therefore, we maximize the electron-hole pair generation and expect more intense PL emission in these geometrical conditions.

The light-matter interaction effectiveness can be enhanced when we introduce this nanocavity design on a plasmonic Nano unit platform. Therefore, these nanocavities are grown on a plasmonic nanoparticle rather than a thick blank Au layer. Again, we simulated a periodic arrangement of spherical particles to simplify the picture, as shown in Figures 5.1(d-e). The periodicity of the unit cell is supposed to be 100 nm, we set the diameter at 50 nm, and the Al_2O_3 and CdSe thicknesses are 20 nm and 6 nm. Next, we examined the electric-field (E-field) distribution across the cavity using FDTD simulations to understand the differences with a planar FP design. The E-field distributions are extracted at 500 nm and 600 nm wavelengths, as shown in Figures 5.1(f-g). These panels clearly show the formation of plasmonic hot spots in the gap region between two plasmonic particles. These hot spots magnify the electron-hole pair generation rate in the CdSe active layer and, therefore, we anticipate

that their consequent PL is enhanced. Considering all, we deduce that different phenomena are responsible for light absorption in a semiconductor-based nanocavity metasurface design based on the design geometries. The plasmonic excitation is weak in a large particle scenario, and the dominant resonance mechanism is FP excitation. However, for sub-wavelength particles, the excitation of plasmon resonance leads to the formation of hot spots. Essentially, the amplitude of these hot spots is inversely proportional to the gap size between two particles. Moreover, a broadband light-matter interaction is required to utilize the total spectrum absorption, and we can achieve this by a multi-sized/multi-spacing plasmonic design. Therefore, in an ideal scenario, multiple geometries disordered near touching, plasmonic nanocavity design can significantly enhance the emission strength of a QD unit.

5.3. Results and Discussions

We used the oblique angle deposition technique using a thermal evaporator to grow Au nanoislands on a quartz substrate to realize this design architecture. Due to the atomic shadowing effect, the layer grows as nanoisland configurations in this method. In this competitive process, the larger islands get even more prominent while suppressing the smaller one's growth due to the complete masking. Therefore, only the largest islands grow in thicker layers, while we can have multiple-sized particles in thinner layers. In addition, we found that, in near touching plasmonic particles, smaller dimensions generate a more substantial field enhancement [13]. Taking all into account, we chose the Au nanoislands heights at a nominal value of 20 nm. In fact, the height, lateral size, and spacing of these particles are all random, as shown in the top and cross-sectional scanning electron microscopy (SEM) images in Figures 5.2(a-b). Atomic force microscopy (AFM) mapping (Figure 5.2(c)) also shows the nature of this randomness in the thickness of the islands. Therefore, a thin but conformal insulator shell layer should grow on these islands to fabricate the nanocavity units (see Figure 5.2(d). The atomic layer deposition (ALD) is the most promising approach to achieving this goal among all the possible routes.

For the ALD growth of an Al_2O_3 coating, we set the chamber temperature at 200°C and $Al(CH_3)_3$ and utilized water precursors as Al and O sources. We chose the pulse and purge times to be 0.015 s and 10 s. We employed transmission electron microscopy (TEM) imaging on the bladed sample to resolve the ultrathin shell layer on gold nanoparticles. Figures 5.2(e) shows the conformal growth of a thin Al_2O_3 shell layer on an Au core. All these structural characterizations prove the successful formation of our targeted plasmonic platform.

Next step, we explore the optical behavior of these random nano units. For this purpose, we measured the reflection and transmission data of the bare Au nanoislands and 20 nm Al_2O_3 coated (the optimal geometry as shown in Figure 5.1(c) one from 400 nm to 700 nm. Later, using the A=1-R-T formula, the absorption spectra are also calculated. All obtained results have been shown in Figure 5.2(f). We can see a near-flat absorption response for both cases from these plots. This flat absorption is due to the multi-size/multi-spacing nature of the fabricated sample that triggers the excitation of plasmonic resonances in a different spectral range. The superposition of these

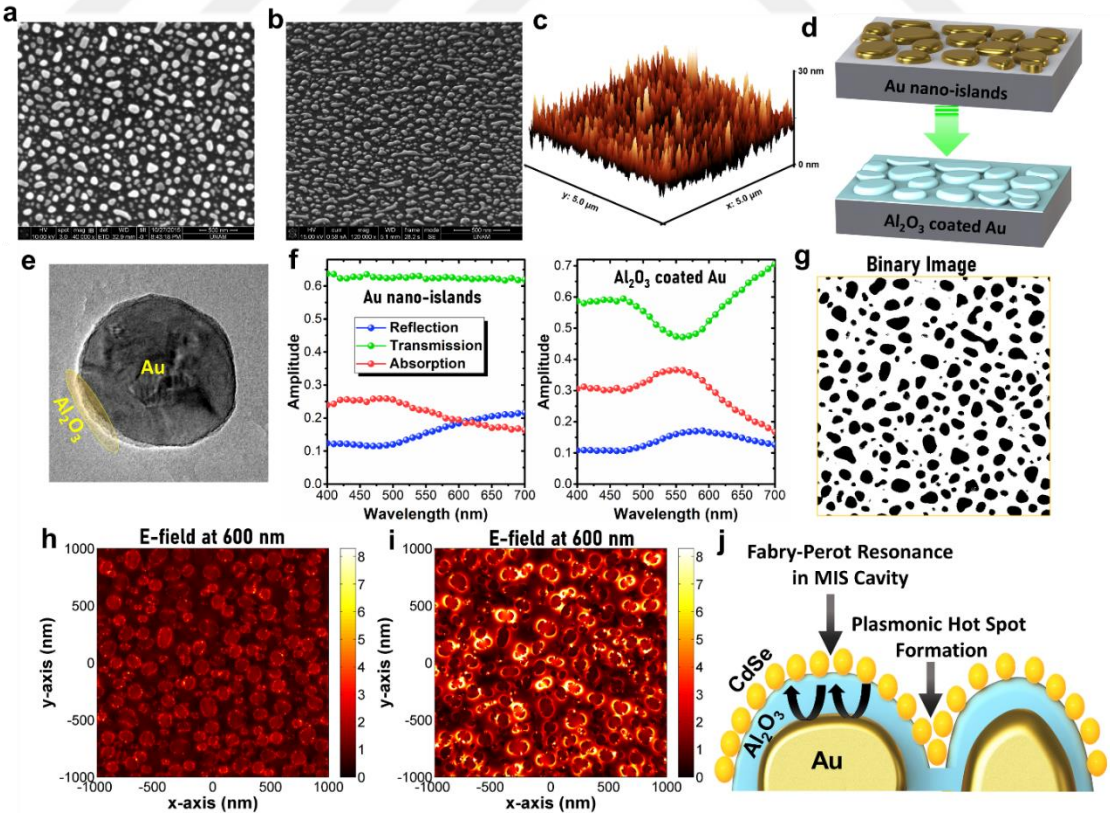

Figure 5.2 The **(a)** top and **(b)** cross-sectional SEM images of the plasmonic nanoislands and **(c)** their AFM image showing the multiple-sized particle formation. **(d)** The schematic view of plasmonic nanoislands and alumina coated nanoislands and **(e)** the TEM image of a particle coated with alumina layer. **(f)** The spectral response of nano-island and alumina-coated nanoislands. **(g)** The binary version of SEM images and their electric field distribution for **(h)** Au nanoisland and **(i)** 20 nm Al_2O_3 coated nanoislands at 600 nm wavelength. **(j)** The involved enhancement mechanisms.

resonant responses lead to a near flat overall profile. Therefore we can anticipate that this plasmonic substrate can provide strong light-matter interaction in the visible range, and the coupling of these amplified near-fields into a QD unit significantly improves its absorption/emission property. Moreover, from these data, an alumina-coated sample has stronger absorption compared to bare Au nanoislands and, therefore, they should impose brighter hot spots in the gap regions. We conducted numerical simulations on the actual sample morphology to verify this assumption. For this aim, we converted the SEM image into a binary image, and then it was imported into a simulation environment as a 20 nm thick layer. Then, we introduce an alumina shell layer to wrap the nano units. Finally, we compare the E-field distribution in a 600 nm wavelength for Au nanoisland and 20 nm Al_2O_3 coated Au nanoisland designs. We set the color bar as the same for both maps. Figure 5.2(h-i) shows that the cavity design has more potent and denser hot spots than the basic design. This result is in line with our findings in Figure 5.2(f). According to all these analysis data, the designed plasmonic MIS cavity can contribute to the QD emission enhancement via two main processes; 1) FP resonance, which is the dominant phenomenon in wavelength scale particles, and 2) plasmonic hot spot formation, which is the leading enhancement mechanism in ultra-small gaps. We have schematically summarized these mechanisms in Figure 5.2(j). Therefore, the fabricated design provides a large-scale compatible route for plasmonic enhanced QD emitters and offers an ideal platform for realizing efficient light-emitting devices.

We transferred a layer of self-assembled QDs onto the plasmonic nanocavity substrate to verify our simulation results. For this aim, a QD layer is

created in a toluene-water interface, using the method explained in previous works [156]. Then, the sample is soaked in the solution to uptake the self-assembled layer on top of the plasmonic substrate. We show this process schematically in Figure 5.3(a). The resultant device has been shown in the SEM image of the surface, see Figure 5.3(b). we completed this process for three sets of samples; i) bare quartz substrate, ii) Au nanoisland-based plasmonic substrate, and iii) Al_2O_3 coated plasmonic MIS cavity-based substrate. In the case of nanocavity design, we fabricated four different alumina thicknesses of 2 nm, 10 nm, 20 nm, and 50 nm. Next, we utilized confocal microscopy imaging to examine the emission strength of these three sets. We chose the excitation wavelength as 530 nm and collected the emission in a broad range spanning from 580 nm to 690 nm. The laser intensity is kept constant throughout all the measurements to have a reliable comparison between all cases. Figure 5.3(c) depicts the confocal image of the samples.

As clearly shown in these panels, the 20 nm thick alumina plasmonic cavity design has a much brighter image than bare and plasmonic ones. Therefore, we collected data from the marked areas with a uniform QD distribution to better compare. The collected PL data is in Figure 5.3(d). From this data, we can deduce that the PL of QD emission has been slightly quenched by the plasmonic design. However, we can tell that it has been significantly amplified (five times) on the plasmonic MIS nanocavity scheme. This amplification is in line with our expectations from the numerical simulations.

As one of the main motivations of this study is proposing a large-scale plasmonic platform for PL enhancement, we performed this experiment in sample size scales. This time, PL spectroscopy (Bruker) is employed to shine the sample with dimensions comparable with the sample size. We plotted the PL spectra of all different samples in Figure 5.3(e). The general trend is similar to what we obtained from the confocal area scan analysis, and this shows the uniformity of the surface morphology of the plasmonic Au nanoislands. When QDs contact gold islands, the non-radiative portion of recombination of excited

electron-hole pairs has been increased (via electron transfer from CdSe conduction band into metal Fermi level). When introducing a 2 nm Al_2O_3 layer between the Au and QD units, the PL has enhanced around three times. Because such ultrathin thickness cannot trigger FP resonant absorption, this improvement is essentially due to suppressing the non-radiative decay of excited electrons. As we move toward the optimal geometry of 20 nm thickness, the intensity increases eight times. In this condition, we have both FP resonance and a plasmonic hot spots mechanism in play, while we have completely suppressed the non-radiative energy transfer. As we move toward thicker layers, FP resonance loses its strength, and the distance between the QD and plasmonic antenna increases, which mitigates the coupling of hot spots into the CdSe layer.

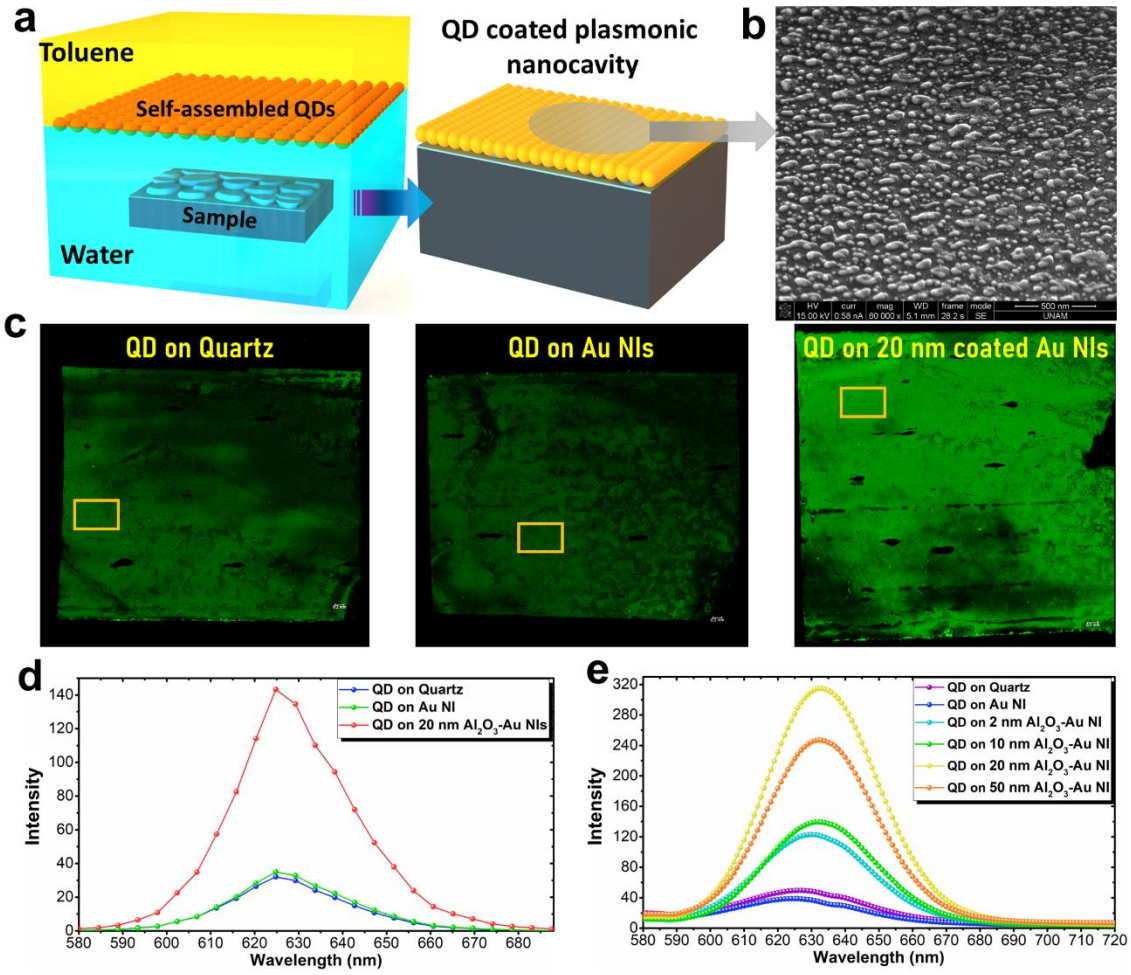

Figure 5.3 **(a)** The graphical explanation of plasmonic nanocavity-QD design formation and **(b)** the resultant device SEM image. **(c)** The confocal images of different samples under 530 nm excitation light, and **(d)** their area PL data. **(e)** The PL spectroscopy data for different designs with 530 nm excitation.

5.1. Summary

This work designed a disordered plasmonic nanocavity design to achieve a nearly eightfold PL enhancement. We found that the multi-scale design geometries of the design trigger the simultaneous formation of FP modes and plasmonic hot spots, thereby leading to a higher electron-hole pair generation rate in a broad wavelength range. This improved absorption consequently leads to higher PL intensities. Besides its efficient operation, the fabrication route of this design is suitable for possible scalable applications.

CHAPTER 6. CONCLUSIONS

6.1. Summary and Outlook

In this thesis work, we designed, fabricated, and characterized two different lithography-free metamaterial platforms to generate and enhance high purity colors. In the first study, we utilized a planar tandem-shaped FP-based cavity to transform the white light into the desired color. Unlike standard FP-based designs that operate in the transmission mode and generally have low efficiencies, the proposed design generates RGB colors in the reflection mode with near-unity amplitude. In the second part of the thesis, we utilized a plasmonic platform to intensify the emission from a quantum dot. In this design, the coupling of hot spots (formed in near-touching units) with the neighboring quantum dots has led to an emission enhancement as substantial as eight times. The primary motivation of this work was to develop and implement large-scale compatible metamaterial architectures to generate high efficiency and high purity visible colors. The proposed design methodology can be used as an extendable toolbox to realize high-performance optical and optoelectronic devices. One of the most promising applications of these lithography-free metamaterial architectures could be photoconversion. Unlike light emission, in photoconversion, we need to enhance the light absorption of the semiconductor using a plasmonic platform. But similar to an emitting system, the formation of hot spots and coupling of these strong fields into a semiconductor unit can significantly enhance its light absorption capacity. This attribute, in turn, leads to substantial enhancement in device photoconversion efficiency. Another area of interest for these platforms could be spectrally selective light photodetection. As the color filters selectively absorb/reflect a specific range of photons, coupling these designs with a photoactive layer can allow the opportunity to realize spectrally selective light photodetection in the visible range. Finally, another application of these metamaterial absorbers is colorimetric sensing. In this sensing platform, the introduction of external stimuli causes a shift in the resonance peak position, and this shows itself as a change in the sample color

which can be distinguished using a naked eye. Further implementation of such a platform with a microfluidic channel could bring this platform into a real-life application.

6.2. Key Challenges and Recommendations

We can discuss the fundamental challenge of these design architectures from two main perspectives; 1) their fabrication route and 2) their optical-electrical performance. From the fabrication perspective, we are still limited by centimeter scales, considering the capacity of the standard fabrication tools. However, we could design and implement custom-made tools to go beyond it and bring these designs into meter scales. For example, using multi-sources in a thermal evaporation tool could provide us the chance to coat samples on large scales with uniform morphologies. The second challenge is the optical-electrical performance of these design platforms. As known in the literature, the optical-electrical properties of thin films made by PVD and CVD approaches are pretty poor compared to single-crystalline bulk designs. This property, in turn, significantly diminishes deposited material performance and reliability for large-scale applications. Implementing post/pre-treatments could improve the structural-optical-electrical performance of these thin films. Moreover, chemical synthesis routes could be an option to realize single-crystalline thin films in dimensions much smaller than the wavelength.

6.3. Contributions

Included in this Thesis

[114] A. C. Kosger, A. Ghobadi, A. R. Rashed, H. Caglayan, and E. Ozbay, “Generation of additive colors with near unity amplitude using a multilayer tandem Fabry–Perot cavity,” *Opt. Lett.*, vol. 46, no. 14, p. 3464, Jul. 2021, doi: 10.1364/OL.430985.

CHAPTER 7. BIBLIOGRAPHY

[1] E. Ozbay, “Plasmonics : Merging Photonics and Electronics at Nanoscale Dimensions,” *Science*, vol. 311, pp. 189–194, 2006, doi: 10.1126/science.1114849.

[2] A. Ghobadi, H. Hajian, B. Butun, and E. Ozbay, “Strong Light-Matter Interaction in Lithography-Free Planar Metamaterial Perfect Absorbers,” *ACS Photonics*, vol. 5, no. 11, pp. 4203–4221, 2018, doi: 10.1021/acsphotonics.8b00872.

[3] J. Toudert, “Spectrally Tailored Light-Matter Interaction in Lithography-Free Functional Nanomaterials,” *Physica Status Solidi (A) Applications and Materials Science*, vol. 217, no. 6, pp. 1–13, 2020, doi: 10.1002/pssa.201900677.

[4] Z. Liu *et al.*, “Automatically Acquired Broadband Plasmonic-Metamaterial Black Absorber during the Metallic Film-Formation,” *ACS Applied Materials & Interfaces*, vol. 7, pp. 4962–4968, 2015, doi: 10.1021/acsami.5b00056.

[5] S. Wang *et al.*, “Large-Area Low-Cost Dielectric Perfect Absorber by One-Step Sputtering,” *Advanced Optical Materials*, vol. 7, no. 9, pp. 1–8, 2019, doi: 10.1002/adom.201801596.

[6] A. Ghobadi, S. A. Dereshgi, H. Hajian, B. Bozok, B. Butun, and E. Ozbay, “Ultra-broadband , wide angle absorber utilizing metal insulator multilayers stack with a multi- thickness metal surface texture,” *Scientific reports*, vol. 7, p. 4755, 2017, doi: 10.1038/s41598-017-04964-3.

[7] A. Ghobadi, H. Hajian, S. A. Dereshgi, B. Bozok, B. Butun, and E. Ozbay, “Disordered Nanohole Patterns in Metal-Insulator Multilayer for Ultra-broadband Light Absorption: Atomic Layer Deposition for Lithography Free Highly repeatable Large Scale Multilayer Growth,” *Scientific Reports*, vol. 7, no. 15079, pp. 1–10, 2017, doi: 10.1038/s41598-017-15312-w.

[8] A. Ghobadi, H. Hajian, A. R. Rashed, B. Butun, and E. Ozbay, “Tuning the metal filling fraction in metal-insulator-metal ultra-broadband perfect absorbers to maximize the absorption bandwidth,” *Photonics Research*, vol. 6, no. 3, pp. 168–176, 2018, doi: 10.1364/PRJ.6.000168.

[9] A. Barranco, A. Borras, A. R. Gonzalez-Elipe, and A. Palmero, “Perspectives on oblique angle deposition of thin films: From fundamentals to devices,” *Progress in Materials Science*, vol. 76, pp. 59–153, Mar. 2016, doi: 10.1016/J.PMATSCI.2015.06.003.

[10] Y. He, J. Fu, and Y. Zhao, “Oblique angle deposition and its applications in plasmonics,” *Frontiers of Physics*, vol. 9, no. 1, pp. 47–59, 2014, doi: 10.1007/s11467-013-0357-1.

[11] D. U. Yildirim *et al.*, “Disordered and Densely Packed ITO Nanorods as an Excellent Lithography-Free Optical Solar Reflector Metasurface,” *ACS Photonics*, vol. 6, no. 7, pp. 1812–1822, 2019, doi: 10.1021/acsphotonics.9b00636.

[12] Z. Eftekhari, A. Ghobadi, and E. Ozbay, “Lithography-free disordered metal–insulator–metal nanoantennas for colorimetric sensing,” *Optics Letters*, vol. 45, no. 24, p. 6719, 2020, doi: 10.1364/ol.410213.

[13] Z. Eftekhari, A. Ghobadi, M. C. Soydan, D. U. Yildirim, N. Cinel, and E. Ozbay, “Strong light emission from a defective hexagonal boron nitride monolayer coupled to near-touching random plasmonic nanounits,” *Optics Letters*, vol. 46, no. 7, p. 1664, 2021, doi: 10.1364/ol.415475.

[14] M. C. Soydan, A. Ghobadi, D. U. Yildirim, V. B. Erturk, and E. Ozbay, “Deep Subwavelength Light Confinement in Disordered Bismuth Nanorods as a Linearly Thermal-Tunable Metamaterial,” *Physica Status Solidi - Rapid Research Letters*, vol. 2000066, pp. 1–6, 2020, doi: 10.1002/pssr.202000066.

[15] J. E. Melzer and E. McLeod, “3D Nanophotonic device fabrication using discrete components,” *Nanophotonics*, vol. 9, no. 6, pp. 1373–1390, 2020, doi: 10.1515/nanoph-2020-0161.

[16] L. Shen *et al.*, “Nanostructured Silicon Photocathodes for Solar Water Splitting Patterned by the Self-Assembly of Lamellar Block Copolymers,” *ACS Applied Materials and Interfaces*, vol. 7, no. 47, pp. 26043–26049, 2015, doi: 10.1021/acsami.5b08661.

[17] X. Ruan *et al.*, “Ultrathin, broadband, omnidirectional, and polarization-independent infrared absorber using all-dielectric refractory materials,” *Nanophotonics*, vol. 10, no. 6, pp. 1683–1690, 2021, doi: 10.1515/nanoph-2020-0627.

[18] H. Robatjazi, S. M. Bahauddin, L. H. Macfarlan, S. Fu, and I. Thomann, “Ultrathin AAO Membrane as a Generic Template for Sub-100 nm Nanostructure Fabrication,” *Chemistry of Materials*, vol. 28, no. 13, pp. 4546–4553, 2016, doi: 10.1021/acs.chemmater.6b00722.

[19] U. T. D. Thuy, N. T. Thuy, N. T. Tung, E. Janssens, and N. Q. Liem, “Large-area cost-effective lithography-free infrared metasurface absorbers for molecular detection,” *APL Materials*, vol. 7, no. 7, 2019, doi: 10.1063/1.5102106.

[20] J. G. Endriz and W. E. Spicer, “SURFACE-PLASMON-ONE-ELECTRON DECAY AND ITS OBSERVATION IN PHOTOEMISSION*,” *Physical Review Letters*, vol. 22, pp. 64–68, 1969.

[21] R. Fuchs and K. L. Kliewer, “Surface Plasmon in a Semi-Infinite Free-Electron Gas,” *Physical Review B*, vol. 3, pp. 2270–2278, 1971.

[22] S. Mubeen, J. Lee, N. Singh, S. Krämer, G. D. Stucky, and M. Moskovits, “An autonomous photosynthetic device in which all charge carriers derive from surface plasmons,” *Nature Nanotechnology*, vol. 8, no. 4, pp. 247–251, 2013, doi: 10.1038/nnano.2013.18.

[23] S. Mukherjee *et al.*, “Hot electrons do the impossible: Plasmon-induced dissociation of H 2 on Au,” *Nano Letters*, vol. 13, no. 1, pp. 240–247, 2013, doi: 10.1021/nl303940z.

[24] Y. Zhang, Y. R. Zhen, O. Neumann, J. K. Day, P. Nordlander, and N. J. Halas, “Coherent anti-Stokes Raman scattering with single-molecule sensitivity using a plasmonic Fano resonance,” *Nature Communications*, vol. 5, pp. 1–7, 2014, doi: 10.1038/ncomms5424.

[25] R. Zhang *et al.*, “Chemical mapping of a single molecule by plasmon-enhanced Raman scattering,” *Nature*, vol. 498, no. 7452, pp. 82–86, 2013, doi: 10.1038/nature12151.

[26] R. M. Ma, S. Ota, Y. Li, S. Yang, and X. Zhang, “Explosives detection in a lasing plasmon nanocavity,” *Nature Nanotechnology*, vol. 9, no. 8, pp. 600–604, 2014, doi: 10.1038/nnano.2014.135.

[27] Y. Fang and M. Sun, “Nanoplasmonic waveguides: Towards applications in integrated nanophotonic circuits,” *Light: Science and Applications*, vol. 4, no. December 2014, pp. 1–11, 2015, doi: 10.1038/lsa.2015.67.

[28] N. I. Zheludev, S. L. Prosvirnin, N. Papasimakis, and V. A. Fedotov, “Lasing spaser,” *Nature Photonics*, vol. 2, no. 6, pp. 351–354, 2008, doi: 10.1038/nphoton.2008.82.

[29] A. Kristensen *et al.*, “Plasmonic colour generation,” *Nature Reviews Materials*, vol. 2, no. 1, p. 16088, 2016, doi: 10.1038/natrevmats.2016.88.

[30] C. Clavero, “Plasmon-induced hot-electron generation at nanoparticle/metal-oxide interfaces for photovoltaic and photocatalytic devices,” *Nature Photonics*, vol. 8, no. 2, pp. 95–103, 2014, doi: 10.1038/nphoton.2013.238.

[31] W. Li and J. G. Valentine, “Harvesting the loss: Surface plasmon-based hot electron photodetection,” *Nanophotonics*, vol. 6, no. 1, pp. 177–191, 2017, doi: 10.1515/nanoph-2015-0154.

[32] T. G. U. Ghobadi, A. Ghobadi, E. Ozbay, and F. Karadas, “Strategies for Plasmonic Hot-Electron-Driven Photoelectrochemical Water Splitting,” *ChemPhotoChem*, vol. 2, pp. 161–182, 2018, doi: 10.1002/cptc.201700165.

[33] A. Ghobadi, H. Hajian, M. Gokbayrak, B. Butun, and E. Ozbay, “Bismuth-based metamaterials: From narrowband reflective color filter to extremely broadband near perfect absorber,” *Nanophotonics*, vol. 8, no. 5, pp. 823–832, 2019, doi: 10.1515/nanoph-2018-0217.

[34] A. Ghobadi, H. Hajian, M. C. Soydan, B. Butun, and E. Ozbay, “Lithography-Free Planar Band-Pass Reflective Color Filter Using Series Connection of Cavities,” *Scientific Reports*, vol. 9, no. 290, pp. 1–11, 2019, doi: 10.1038/s41598-018-36540-8.

[35] S. Abedini Dereshgi, A. Ghobadi, H. Hajian, B. Butun, and E. Ozbay, “Ultra-Broadband, Lithography-Free, and Large-Scale Compatible Perfect Absorbers: The Optimum Choice of Metal layers in Metal-Insulator Multilayer Stacks,” *Scientific Reports*, vol. 7, no. 1, p. 14872, 2017, doi: 10.1038/s41598-017-13837-8.

[36] H. Hajian, A. Ghobadi, B. Butun, and E. Ozbay, “Nearly perfect resonant absorption and coherent thermal emission by hBN-based photonic crystals,” *Optics Express*, vol. 25, no. 25, pp. 31970–31987, 2017, doi: 10.1364/OE.25.031970.

[37] A. Ghobadi *et al.*, “97 percent light absorption in an ultrabroadband frequency range utilizing an ultrathin metal layer: Randomly oriented, densely packed dielectric nanowires as an excellent light trapping scaffold,” *Nanoscale*, vol. 9, no. 43, pp. 16652–16660, 2017, doi: 10.1039/c7nr04186a.

[38] A. Ghobadi, Y. Demirag, H. Hajian, A. Toprak, B. Butun, and E. Ozbay, “Spectrally Selective Ultrathin Photodetectors Using Strong Interference in Nanocavity Design,” *IEEE Electron Device Letters*, vol. 40, no. 6, pp. 1–1, 2019, doi: 10.1109/led.2019.2910064.

[39] C. Ji, K. T. Lee, T. Xu, J. Zhou, H. J. Park, and L. J. Guo, “Engineering Light at the Nanoscale: Structural Color Filters and Broadband Perfect Absorbers,” *Advanced Optical Materials*, vol. 5, no. 20, p. 1700368, 2017, doi: 10.1002/adom.201700368.

[40] S. Ogawa and M. Kimata, “Metal-Insulator-Metal-Based Plasmonic Metamaterial Absorbers at Visible and Infrared Wavelengths: A Review,” *Materials*, vol. 11, no. 458, pp. 1–18, 2018, doi: 10.3390/ma11030458.

[41] N. Liu, M. Mesch, T. Weiss, M. Hentschel, and H. Giessen, “Infrared perfect absorber and its application as plasmonic sensor,” *Nano Letters*, vol. 10, no. 7, pp. 2342–2348, 2010, doi: 10.1021/nl9041033.

[42] K. Aydin, V. E. Ferry, R. M. Briggs, and H. a. Atwater, “Broadband polarization-independent resonant light absorption using ultrathin plasmonic super absorbers,” *Nature Communications*, vol. 2, no. 517, pp. 1–7, 2011, doi: 10.1038/ncomms1528.

[43] J. Hao, J. Wang, X. Liu, W. J. Padilla, L. Zhou, and M. Qiu, “High performance optical absorber based on a plasmonic metamaterial,” *Applied Physics Letters*, vol. 96, p. 251104, 2010, doi: 10.1063/1.3442904.

[44] M. K. Hedayati *et al.*, “Design of a perfect black absorber at visible frequencies using plasmonic metamaterials,” *Advanced Materials*, vol. 23, no. 45, pp. 5410–5414, 2011, doi: 10.1002/adma.201102646.

[45] J. Hao, L. Zhou, and M. Qiu, “Nearly total absorption of light and heat generation by plasmonic metamaterials,” *Physical Review B*, vol. 83, p. 165107, 2011, doi: 10.1103/PhysRevB.83.165107.

[46] C. M. Watts, X. Liu, and W. J. Padilla, “Metamaterial Electromagnetic Wave Absorbers,” *Advanced optical materials*, vol. 24, pp. OP98–OP120, 2012, doi: 10.1002/adma.201200674.

[47] S. Shu, Z. Li, and Y. Y. Li, “Triple-layer Fabry-Perot absorber with near-perfect absorption in visible and near-infrared regime,” *Optics Express*, vol. 21, no. 21, pp. 4795–4801, 2013, doi: 10.1364/OE.21.025307.

[48] Y. S. Do and K. C. Choi, “Poly-periodic hole arrays for angle-invariant plasmonic filters,” *Optics Letters*, vol. 40, no. 16, pp. 3873–3876, 2015.

[49] A. Moreau *et al.*, “Controlled-reflectance surfaces with film-coupled colloidal nanoantennas,” *Nature*, vol. 492, pp. 86–90, 2012, doi: 10.1038/nature11615.

[50] A. Cattoni, P. Ghenuche, D. Decanini, J. Chen, and J. Pelouard, “λ3/1000 Plasmonic Nanocavities for Biosensing Fabricated by Soft UV Nanoimprint Lithography,” *Nano Letters*, vol. 11, pp. 3557–3563, 2011, doi: 10.1021/nl201004c.

[51] N. Zhang *et al.*, “Reversibly tunable coupled and decoupled super absorbing structures,” *Applied Physics Letters*, vol. 108, p. 091105, 2016, doi: 10.1063/1.4943089.

[52] N. I. Landy, S. Sajuyigbe, J. J. Mock, D. R. Smith, and W. J. Padilla, “Perfect Metamaterial Absorber,” *Physical Review Letters*, vol. 100, p. 207402, 2008, doi: 10.1103/PhysRevLett.100.207402.

[53] W. Chang, J. Won, L. S. Slaughter, and S. Link, “Plasmonic nanorod absorbers as orientation sensors,” *PNAS*, vol. 107, no. 7, pp. 2781–2786, 2010, doi: 10.1073/pnas.0910127107.

[54] Y. Avitzour, Y. A. Urzhumov, and G. Shvets, “Wide-angle infrared absorber based on a negative-index plasmonic metamaterial,” *Physical Review B*, vol. 79, no. 4, pp. 1–5, 2009, doi: 10.1103/PhysRevB.79.045131.

[55] Q. Wen, Y. Xie, H. Zhang, Q. Yang, and Y. Li, “Transmission line model and fields analysis of metamaterial absorber in the terahertz band,” *Optics Express*, vol. 17, no. 22, pp. 20256–20265, 2009.

[56] M. Yan, “Metal-insulator-metal light absorber: a continuous structure,” *Journal of Optics*, vol. 15, no. 2, p. 25006(1–8), 2013, doi: 10.1088/2040-8978/15/2/025006.

[57] H. Tao *et al.*, “A dual band terahertz metamaterial absorber,” *Journal of Physics D: Applied Physics*, vol. 43, p. 225102, 2010, doi: 10.1088/0022-3727/43/22/225102.

[58] Z. Yong, S. Zhang, C. Gong, and S. He, “Narrow band perfect absorber for maximum localized magnetic and electric field enhancement and sensing applications,” *Scientific Reports*, vol. 6, p. 24063, 2016, doi: 10.1038/srep24063.

[59] P. Mandal, “plasmonic metamaterial perfect absorber at visible frequency : design rule,” *Journal of Nanophotonics*, vol. 11, no. 3, p. 036003, 2017, doi: 10.1117/1.JNP.11.036003.

[60] B. Wang, W.-Q. Huang, and L.-L. Wang, “Ultra-narrow terahertz perfect light absorber based on surface lattice resonance of a sandwich resonator for sensing applications,” *RSC Advances*, vol. 7, pp. 42956–42963, 2017, doi: 10.1039/C7RA08413G.

[61] D. Wu *et al.*, “Infrared Perfect Ultra-narrow Band Absorber as Plasmonic Sensor,” *Nanoscale Research Letters*, vol. 11, no. 1, p. 483, 2016, doi: 10.1186/s11671-016-1705-1.

[62] J. Kim, K. Han, and J. W. Hahn, “Selective dual-band metamaterial perfect absorber for infrared stealth technology,” *Scientific Reports*, vol. 7, p. 6740, 2017, doi: 10.1038/s41598-017-06749-0.

[63] X. Liu, T. Starr, A. F. Starr, and W. J. Padilla, “Infrared Spatial and Frequency Selective Metamaterial with Near-Unity Absorbance,” *Physical Review Letters*, vol. 104, p. 207403, 2010, doi: 10.1103/PhysRevLett.104.207403.

[64] H. Wang and L. Wang, “Perfect selective metamaterial solar absorbers,” *Optics Express*, vol. 21, no. S6, pp. 13311–13319, 2013, doi: 10.1364/OE.21.0A1078.

[65] M. G. Nielsen, A. Pors, O. Albrektsen, and S. I. Bozhevolnyi, “Efficient absorption of visible radiation by gap plasmon resonators,” *Optics Express*, vol. 20, no. 12, pp. 13311–13319, 2012.

[66] X. Ming and Q. Tan, “Design Method of a Broadband Wide-Angle Plasmonic Absorber in the Visible Range,” *Plasmonics*, vol. 12, no. 1, pp. 14–17, 2017, doi: 10.1007/s11468-016-0236-z.

[67] M. Kenney, J. Grant, Y. D. Shah, I. Escorcia-carranza, M. Humphreys, and D. R. S. Cumming, “Octave-Spanning Broadband Absorption of Terahertz Light Using Metasurface Fractal-Cross Absorbers,” *ACS Photonics*, vol. 4, pp. 2604–2612, 2017, doi: 10.1021/acsphotonics.7b00906.

[68] X. Duan, S. Chen, W. Liu, H. Cheng, and Z. Li, “Polarization-insensitive and wide-angle broadband nearly perfect absorber by tunable planar metamaterials in the visible regime,” *Journal of Optics*, vol. 16, p. 125107, 2014, doi: 10.1088/2040-8978/16/12/125107.

[69] A. K. Azad *et al.*, “Metasurface Broadband Solar Absorber,” *Scientific Reports*, vol. 6, p. 20347, 2016, doi: 10.1038/srep20347.

[70] R. Mudachathi and T. Tanaka, “Broadband plasmonic perfect light absorber in the visible spectrum for solar cell applications,” *Advances in Natural Sciences: Nanoscience and Nanotechnology*, vol. 9, p. 015010, 2018.

[71] Y. Lu, W. Dong, Z. Chen, A. Pors, Z. Wang, and S. I. Bozhevolnyi, “Gap-plasmon based broadband absorbers for enhanced hot- electron and photocurrent generation,” *Scientific Reports*, vol. 6, p. 30650, 2016, doi: 10.1038/srep30650.

[72] G. Tagliabue, H. Eghlidi, and D. Poulikakos, “Facile multifunctional plasmonic sunlight harvesting with tapered triangle nanopatterning of thin films.,” *Nanoscale*, vol. 5, no. 20, pp. 9957–62, 2013, doi: 10.1039/c3nr03273f.

[73] A. Ghobadi *et al.*, “Visible light nearly perfect absorber: an optimum unit cell arrangement for near absolute polarization insensitivity,” *Optics Express*, vol. 25, no. 22, p. 27624, 2017, doi: 10.1364/OE.25.027624.

[74] T. Ji, Y. Wang, Y. Cui, Y. Lin, Y. Hao, and D. Li, “Flexible broadband plasmonic absorber on moth-eye substrate,” *Materials Today Energy*, vol. 5, pp. 181–186, 2017, doi: 10.1016/j.mtener.2017.06.010.

[75] J. A. Bossard, L. Lin, S. Yun, L. Liu, D. H. Werner, and T. S. Mayer, “Near-Ideal Optical Metamaterial Absorbers with Super-Octave Bandwidth,” *ACS Nano*, vol. 8, no. 2, pp. 1517–1524, 2014, doi: 10.1021/nn4057148.

[76] F. Ding, J. Dai, Y. Chen, J. Zhu, Y. Jin, and S. I. Bozhevolnyi, “Broadband near-infrared metamaterial absorbers utilizing highly lossy metals,” *Scientific Reports*, vol. 6, p. 39445, 2016, doi: 10.1038/srep39445.

[77] C. S. Park, V. R. Shrestha, S. S. Lee, and D. Y. Choi, “Trans-Reflective Color Filters Based on a Phase Compensated Etalon Enabling Adjustable Color Saturation,” *Scientific Reports*, vol. 6, p. 25496, 2016, doi: 10.1038/srep25496.

[78] Z. Li, S. Butun, and K. Aydin, “Large-area, Lithography-free super absorbers and color filters at visible frequencies using ultrathin metallic films,” *ACS Photonics*, vol. 2, no. 2, pp. 183–188, 2015, doi: 10.1021/ph500410u.

[79] K. Mao *et al.*, “Angle insensitive color filters in transmission covering the visible region,” *Scientific Reports*, vol. 6, p. 19289, 2016, doi: 10.1038/srep19289.

[80] C. S. Park, V. R. Shrestha, S. S. Lee, E. S. Kim, and D. Y. Choi, “Omnidirectional color filters capitalizing on a nano-resonator of Ag-TiO2 -Ag integrated with a phase compensating dielectric overlay,” *Scientific Reports*, vol. 5, p. 8467, 2015, doi: 10.1038/srep08467.

[81] K.-T. Lee, S. Seo, J. Y. Lee, and L. J. Guo, “Strong resonance effect in a lossy medium-based optical cavity for angle robust spectrum filters.,” *Advanced materials*, vol. 26, no. 36, pp. 6324–6328, 2014, doi: 10.1002/adma.201402117.

[82] J. H. Han, D.-Y. Kim, D. Kim, and K. C. Choi, “Highly conductive and flexible color filter electrode using multilayer film structure,” *Scientific Reports*, vol. 6, p. 29341, 2016, doi: 10.1038/srep29341.

[83] K. T. Lee, S. Seo, J. Yong Lee, and L. Jay Guo, “Ultrathin metal-semiconductor-metal resonator for angle invariant visible band transmission filters,” *Applied Physics Letters*, vol. 104, p. 231112, 2014, doi: 10.1063/1.4883494.

[84] C. Yang *et al.*, “Compact multilayer film structure for angle insensitive color filtering,” *Scientific Reports*, vol. 5, p. 9285, 2015, doi: 10.1038/srep09285.

[85] K. T. Lee, S. Y. Han, and H. J. Park, “Omnidirectional Flexible Transmissive Structural Colors with High-Color-Purity and High-Efficiency Exploiting Multicavity Resonances,” *Advanced Optical Materials*, vol. 5, no. 14, p. 1700284, 2017, doi: 10.1002/adom.201700284.

[86] Z. Li, S. Butun, and K. Aydin, “Lithography-free transmission fi lters at ultraviolet frequencies using ultra-thin aluminum films,” *Journal of Optics*, vol. 18, p. 065006, 2016, doi: 10.1088/2040-8978/18/6/065006.

[87] Y. Zhao *et al.*, “Artificial structural color pixels: A review,” *Materials*, vol. 10, p. 944, 2017, doi: 10.3390/ma10080944.

[88] Y.-T. Yoon and S.-S. Lee, “Transmission type color filter incorporating a silver film based etalon.,” *Optics express*, vol. 18, no. 5, pp. 5344–5349, 2010, doi: 10.1364/OE.18.005344.

[89] D. Zhao *et al.*, “Ultra-narrow-band light dissipation by a stack of lamellar silver and alumina,” *Applied Physics Letters*, vol. 104, p. 221107, 2014, doi: 10.1063/1.4881267.

[90] J. Y. Lee, K. T. Lee, S. Seo, and L. J. Guo, “Decorative power generating panels creating angle insensitive transmissive colors,” *Scientific Reports*, vol. 4, p. 4192, 2014, doi: 10.1038/srep04192.

[91] S. S. Mirshafieyan and D. A. Gregory, “Electrically tunable perfect light absorbers as color filters and modulators,” *Scientific Reports*, no. January, pp. 1–9, 2018, doi: 10.1038/s41598-018-20879-z.

[92] H. A. O. P. Eng, Y. I. L. Uo, X. I. Y. Ing, Y. P. U. Ang, Y. A. J. Iang, and J. X. U. Immy, “Broadband and highly absorbing multilayer structure in mid-infrared,” *Applied Optics*, vol. 55, no. 31, pp. 8833–8838, 2016.

[93] Z. Li, E. Palacios, S. Butun, H. Kocer, and K. Aydin, “Omnidirectional, broadband light absorption using large-area, ultrathin lossy metallic film coatings,” *Scientific Reports*, vol. 5, no. 15137, pp. 1–22, 2015, doi: 10.1038/srep15137.

[94] A. Ghobadi, S. A. Dereshgi, B. Butun, and E. Ozbay, “Ultra-broadband Asymmetric Light Transmission and Absorption Through The Use of Metal Free Multilayer Capped Dielectric Microsphere Resonator,” *Scientific Reports*, vol. 7, p. 14538, 2017, doi: 10.1038/s41598-017-15248-1.

[95] N. Mattiucci, M. J. Bloemer, N. Akozbek, and G. D’Aguanno, “Impedance matched thin metamaterials make metals absorbing,” *Scientific Reports*, vol. 3, no. 3203, pp. 1–11, 2013, doi: 10.1038/srep03203.

[96] M. Chirumamilla *et al.*, “Multilayer tungsten-alumina-based broadband light absorbers for high-temperature applications,” *Optical Materials Express*, vol. 6, no. 8, p. 2704, 2016, doi: 10.1364/OME.6.002704.

[97] H. Deng, Z. Li, L. Stan, D. Rosenmann, and D. Czaplewski, “Broadband perfect absorber based on one ultrathin layer of refractory metal,” *Optics Letters*, vol. 40, no. 11, pp. 2592–2595, 2015.

[98] G. Kajtár, M. Kafesaki, E. N. Economou, and C. M. Soukoulis, “Theoretical model of homogeneous metal–insulator–metal perfect multi-band absorbers for the visible spectrum,” *Journal of Physics D: Applied Physics*, vol. 49, no. 5, p. 055104, 2016, doi: 10.1088/0022-3727/49/5/055104.

[99] F. Ding *et al.*, “Lithography-free, broadband, omnidirectional, and polarization-insensitive thin optical absorber,” *Applied Physics Letters*, vol. 106, p. 061108, 2015, doi: 10.1063/1.4908182.

[100] Y. K. Zhong *et al.*, “Omnidirectional, polarization-independent, ultra-broadband metamaterial perfect absorber using field-penetration and

reflected-wave-cancellation," *Optics Express*, vol. 24, no. 10, p. A832, 2016, doi: 10.1364/OE.24.00A832.

[101] Y. K. Zhong *et al.*, "Fully Planarized Perfect Metamaterial Absorbers With No Photonic Nanostructures," *IEEE Photonics Journal*, vol. 8, no. 1, p. 2200109, 2016, doi: 10.1109/JPHOT.2015.2507368.

[102] S. M. Fu, Y. K. Zhong, M. H. Tu, B. R. Chen, and A. Lin, "A fully functionalized metamaterial perfect absorber with simple design and implementation," *Scientific Reports*, vol. 6, p. 36244, 2016, doi: 10.1038/srep36244.

[103] S. Abedini Dereshgi, A. Ghobadi, H. Hajian, B. Butun, and E. Ozbay, "Ultra-Broadband, Lithography-Free, and Large-Scale Compatible Perfect Absorbers: The Optimum Choice of Metal layers in Metal-Insulator Multilayer Stacks," *Scientific Reports*, vol. 7, no. 1, 2017, doi: 10.1038/s41598-017-13837-8.

[104] A. Ghobadi, H. Hajian, A. R. Rashed, B. Butun, and E. Ozbay, "Tuning the metal filling fraction in absorbers to maximize the absorption bandwidth," *Photonics Reseach*, vol. 6, no. 3, pp. 168–176, 2018.

[105] H. A. Atwater and A. Polman, "Plasmonics for improved photovoltaic devices," *Nature Materials*, vol. 9, no. 10, pp. 865–865, 2010, doi: 10.1038/nmat2866.

[106] S. A. Maier and H. A. Atwater, "Plasmonics: Localization and guiding of electromagnetic energy in metal/dielectric structures," *Journal of Applied Physics*, vol. 98, no. 1, pp. 1–10, 2005, doi: 10.1063/1.1951057.

[107] I. S. I. Web, S. This, H. Press, N. York, and A. Nw, "Plasmonics: Merging Photonics and Electronics at Nanoscale Dimensions," *Science*, vol. 189, no. 2006, pp. 189–194, 2012, doi: 10.1126/science.1114849.

[108] W. R. Erwin, H. F. Zarick, E. M. Talbert, and R. Bardhan, "Light trapping in mesoporous solar cells with plasmonic nanostructures," *Energy Environ. Sci.*, vol. 9, pp. 1577–1601, 2016, doi: 10.1039/C5EE03847B.

[109] K. Islam, A. Alnuaimi, E. Battal, A. K. Okyay, and A. Nayfeh, "Effect of gold nanoparticles size on light scattering for thin film amorphous-silicon solar cells," *Solar Energy*, vol. 103, pp. 263–268, 2014, doi: 10.1016/j.solener.2014.02.023.

[110] B. J. Soller and D. G. Hall, "Scattering enhancement from an array of interacting dipoles near a planar waveguide," *Journal of the Optical Society of America B*, vol. 19, no. 10, p. 2437, 2002, doi: 10.1364/JOSAB.19.002437.

[111] C. S. Kumarasinghe, M. Premaratne, Q. Bao, and G. P. Agrawal, "Theoretical analysis of hot electron dynamics in nanorods," *Scientific Reports*, vol. 5, p. 12140, 2015, doi: 10.1038/srep12140.

[112] W. R. Erwin, A. Coppola, H. F. Zarick, P. Arora, K. J. Miller, and R. Bardhan, “Plasmon enhanced water splitting mediated by hybrid bimetallic Au-Ag core-shell nanostructures,” *Nanoscale*, vol. 6, no. 21, pp. 12626–34, 2014, doi: 10.1039/c4nr03625e.

[113] A. Sousa-Castillo *et al.*, “Boosting Hot Electron-Driven Photocatalysis through Anisotropic Plasmonic Nanoparticles with Hot Spots in Au-TiO2 Nanoarchitectures,” *Journal of Physical Chemistry C*, vol. 120, no. 21, pp. 11690–11699, 2016, doi: 10.1021/acs.jpcc.6b02370.

[114] A. C. Kosger, A. Ghobadi, A. R. Rashed, H. Caglayan, and E. Ozbay, “Generation of additive colors with near unity amplitude using a multilayer tandem Fabry–Perot cavity,” *Opt. Lett.*, vol. 46, no. 14, p. 3464, Jul. 2021, doi: 10.1364/OL.430985.

[115] C. Ji, K. T. Lee, T. Xu, J. Zhou, H. J. Park, and L. J. Guo, “Engineering Light at the Nanoscale: Structural Color Filters and Broadband Perfect Absorbers,” *Advanced Optical Materials*, vol. 5, no. 20, pp. 1–22, 2017, doi: 10.1002/adom.201700368.

[116] D. Fleischman, L. A. Sweatlock, H. Murakami, and H. Atwater, “Hyper-selective plasmonic color filters,” *Optics Express*, vol. 25, no. 22, pp. 27386–27395, 2017, doi: 10.1364/OE.25.027386.

[117] I. Koirala, V. R. Shrestha, C. S. Park, S. S. Lee, and D. Y. Choi, “Polarization-Controlled Broad Color Palette Based on an Ultrathin One-Dimensional Resonant Grating Structure,” *Scientific Reports*, vol. 7, p. 40073, 2017, doi: 10.1038/srep40073.

[118] Y. Gu, L. Zhang, J. K. W. Yang, S. P. Yeo, and C.-W. Qiu, “Color generation *via* subwavelength plasmonic nanostructures,” *Nanoscale*, vol. 7, no. 15, pp. 6409–6419, 2015, doi: 10.1039/C5NR00578G.

[119] Q. Xiang, Y. Chen, and Y. Wang, “Plasmonic reflection color filters with metallic random nanostructures,” *NANOTECHNOLOGY*, vol. 28, p. 085203, 2017.

[120] J. Wang *et al.*, “Ultra-thin plasmonic color filters incorporating free-standing resonant membrane waveguides with high transmission efficiency,” *Applied Physics Letters*, vol. 110, no. 3, p. 031110, 2017, doi: 10.1063/1.4974455.

[121] Y.-T. Yoon, H.-S. Lee, S.-S. Lee, S. H. Kim, J.-D. Park, and K.-D. Lee, “Color filter incorporating a subwavelength patterned grating in poly silicon.,” *Optics express*, vol. 16, no. 4, pp. 2374–2380, 2008, doi: 10.1364/OE.16.002374.

[122] M. J. Uddin, T. Khaleque, and R. Magnusson, “Guided-mode resonant polarization-controlled tunable color filters,” *Optics Express*, vol. 22, no. 10, pp. 12307–12315, 2014, doi: 10.1364/OE.22.012307.

[123] M. J. Uddin and R. Magnusson, “Efficient guided-mode-resonant tunable color filters,” *IEEE Photonics Technology Letters*, vol. 24, no. 17, pp. 1552–1554, 2012, doi: 10.1109/LPT.2012.2208453.

[124] Q. Wang *et al.*, “Colored image produced with guided-mode resonance filter array,” *Optics Letters*, vol. 36, no. 23, pp. 4698–4700, 2011, doi: 10.1364/OL.36.004698.

[125] C.-T. Wang, P.-C. Chang, J. J. Lin, M. C. Tai, Y.-J. Hung, and T.-H. Lin, “Full-color reflector using vertically stacked liquid crystal guided-mode resonators,” *Applied Optics*, vol. 25, no. 2, pp. 1248–1252, 2017, doi: 10.1364/AO.56.004219.

[126] E.-H. Cho *et al.*, “Two-dimensional photonic crystal color filter development,” *Optics Express*, vol. 17, no. 10, pp. 8621–8629, 2009, doi: 10.1364/OE.17.008621.

[127] H. Cho *et al.*, “Self-assembled stretchable photonic crystal for a tunable color filter,” *Optics Letters*, vol. 43, no. 15, p. 3501, 2018, doi: 10.1364/ol.43.003501.

[128] W. Yue, S. Gao, S. S. Lee, E. S. Kim, and D. Y. Choi, “Subtractive Color Filters Based on a Silicon-Aluminum Hybrid-Nanodisk Metasurface Enabling Enhanced Color Purity,” *Scientific Reports*, vol. 6, p. 29756, 2016, doi: 10.1038/srep29756.

[129] K.-T. Lee, J.-Y. Jang, S. J. Park, C. Ji, L. J. Guo, and H. J. Park, “Subwavelength nanocavity for flexible structural transmissive color generation with a wide viewing angle,” *Optica*, vol. 3, no. 12, pp. 1489–1495, 2016, doi: 10.1364/OPTICA.3.001489.

[130] A. Ghobadi, H. Hajian, B. Butun, and E. Ozbay, “Strong Light-Matter Interaction in Lithography-Free Planar Metamaterial Perfect Absorbers,” *ACS Photonics*, vol. 5, no. 11, pp. 4203–4221, 2018, doi: 10.1021/acsphotonics.8b00872.

[131] C. Williams, G. Rughoobur, A. J. Flewitt, and T. D. Wilkinson, “Single-step fabrication of thin-film linear variable bandpass filters based on metal–insulator–metal geometry,” *Applied Optics*, vol. 55, no. 32, pp. 9237–9241, 2016, doi: 10.1364/AO.55.009237.

[132] V. R. Shrestha, S. S. Lee, E. S. Kim, and D. Y. Choi, “Non-iridescent transmissive structural color filter featuring highly efficient transmission and high excitation purity,” *Scientific Reports*, vol. 4, p. 4921, 2014, doi: 10.1038/srep04921.

[133] A. Ghobadi, H. Hajian, M. Gokbayrak, B. Butun, and E. Ozbay, “Bismuth-based metamaterials: From narrowband reflective color filter to extremely broadband near perfect absorber,” *Nanophotonics*, vol. 8, no. 5, pp. 823–832, 2019, doi: 10.1515/nanoph-2018-0217.

[134] Z. Yang *et al.*, “Reflective Color Filters and Monolithic Color Printing Based on Asymmetric Fabry–Perot Cavities Using Nickel as a Broadband Absorber,” *Advanced Optical Materials*, vol. 4, no. 8, pp. 1196–1202, 2016, doi: 10.1002/adom.201600110.

[135] A. Ghobadi, H. Hajian, M. C. Soydan, B. Butun, and E. Ozbay, “Lithography-Free Planar Band-Pass Reflective Color Filter Using A Series Connection of Cavities,” *Scientific Reports*, vol. 9, no. 1, 2019, doi: 10.1038/s41598-018-36540-8.

[136] C. Ji, K.-T. Lee, and L. J. Guo, “High-color-purity, angle-invariant, and bidirectional structural colors based on higher-order resonances,” *Optics Letters*, vol. 44, no. 1, p. 86, 2019, doi: 10.1364/ol.44.000086.

[137] “Lumerical Solut. Inc. http://www.lumerical.com/tcad-products/fdtd/.”

[138] Palik, “E. D. Handbook of optical constants of solids. Vol. 3 (Academic press, 1998)”.

[139] M. Achermann, “Exciton-plasmon interactions in metal-semiconductor nanostructures,” *Journal of Physical Chemistry Letters*, vol. 1, no. 19, pp. 2837–2843, 2010, doi: 10.1021/jz101102e.

[140] G. Lamri *et al.*, “Photochromic control of a plasmon-quantum dots coupled system,” *Nanoscale*, vol. 11, no. 1, pp. 258–265, 2019, doi: 10.1039/c8nr08076c.

[141] O. Bitton, S. N. Gupta, and G. Haran, “Quantum dot plasmonics: From weak to strong coupling,” *Nanophotonics*, vol. 8, no. 4, pp. 559–575, 2019, doi: 10.1515/nanoph-2018-0218.

[142] T. B. Hoang, G. M. Akselrod, C. Argyropoulos, J. Huang, D. R. Smith, and M. H. Mikkelsen, “Ultrafast spontaneous emission source using plasmonic nanoantennas,” *Nature Communications*, vol. 6, 2015, doi: 10.1038/ncomms8788.

[143] Y. Wu, S. Ren, X. Xu, L. Liu, H. Wang, and J. Yu, “Engineered fluorescence of quantum dots via plasmonic nanostructures,” *Solar Energy Materials and Solar Cells*, vol. 126, pp. 113–119, 2014, doi: 10.1016/j.solmat.2014.03.050.

[144] M. Praveena, A. Mukherjee, M. Venkatapathi, and J. K. Basu, “Plasmon-mediated emergence of collective emission and enhanced quantum efficiency in quantum dot films,” *Physical Review B - Condensed Matter and Materials Physics*, vol. 92, no. 23, pp. 1–5, 2015, doi: 10.1103/PhysRevB.92.235403.

[145] L. Hu *et al.*, “Plasmon-enhanced surface-state emission of CdSe quantum dots and its application to microscale luminescence patterns,” *Journal of Physical Chemistry C*, vol. 116, no. 20, pp. 11283–11291, 2012, doi: 10.1021/jp210269m.

[146] V. Krivenkov, P. Samokhvalov, I. Nabiev, and Y. P. Rakovich, “Synergy of Excitation Enhancement and the Purcell Effect for Strong Photoluminescence Enhancement in a Thin-Film Hybrid Structure Based on Quantum Dots and Plasmon Nanoparticles,” *J. Phys. Chem. Lett.*, vol. 11, no. 19, pp. 8018–8025, Oct. 2020, doi: 10.1021/acs.jpclett.0c02296.

[147] J.-H. Song, T. Atay, S. Shi, H. Urabe, and A. V. Nurmikko, “Large Enhancement of Fluorescence Efficiency from CdSe/ZnS Quantum Dots Induced by Resonant Coupling to Spatially Controlled Surface Plasmons,” *Nano Lett.*, vol. 5, no. 8, pp. 1557–1561, Aug. 2005, doi: 10.1021/nl050813r.

[148] S. Dey and J. Zhao, “Plasmonic Effect on Exciton and Multiexciton Emission of Single Quantum Dots,” *J. Phys. Chem. Lett.*, vol. 7, no. 15, pp. 2921–2929, Aug. 2016, doi: 10.1021/acs.jpclett.6b01164.

[149] Y. Chen *et al.*, “Excitation enhancement of CdSe quantum dots by single metal nanoparticles,” *Appl. Phys. Lett.*, vol. 93, no. 5, p. 053106, Aug. 2008, doi: 10.1063/1.2956391.

[150] G. M. Akselrod *et al.*, “Probing the mechanisms of large Purcell enhancement in plasmonic nanoantennas,” *Nature Photonics*, vol. 8, no. 11, pp. 835–840, 2014, doi: 10.1038/nphoton.2014.228.

[151] M. Pelton, “Modified spontaneous emission in nanophotonic structures,” *Nature Photonics*, vol. 9, no. 7, pp. 427–435, 2015, doi: 10.1038/nphoton.2015.103.

[152] J. A. Schuller, E. S. Barnard, W. Cai, Y. C. Jun, J. S. White, and M. L. Brongersma, “Plasmonics for extreme light concentration and manipulation,” *Nature Materials*, vol. 9, no. 3, pp. 193–204, 2010, doi: 10.1038/nmat2630.

[153] K. Yuan *et al.*, “Effects of localized surface plasmon resonance of Ag nanoparticles on luminescence of carbon dots with blue, green and yellow emission,” *Applied Surface Science*, vol. 502, no. September 2019, p. 144277, 2020, doi: 10.1016/j.apsusc.2019.144277.

[154] R. Carminati, J. J. Greffet, C. Henkel, and J. M. Vigoureux, “Radiative and non-radiative decay of a single molecule close to a metallic nanoparticle,” *Optics Communications*, vol. 261, no. 2, pp. 368–375, 2006, doi: 10.1016/j.optcom.2005.12.009.

[155] J. Kümmerlen, A. Leitner, H. Brunner, F. R. Aussenegg, and A. Wokaun, “Enhanced dye fluorescence over silver island films: analysis of the distance dependence,” *Molecular Physics*, vol. 80, no. 5, pp. 1031–1046, Dec. 1993, doi: 10.1080/00268979300102851.

[156] Z. Yu, C. F. Wang, and S. Chen, “Fabrication of quantum dot-based photonic materials from small to large via interfacial self-assembly,”

Journal of Materials Chemistry, vol. 21, no. 24, pp. 8496–8501, 2011, doi: 10.1039/c1jm10281h.